



Congregated-electrons-strengthened anchoring and mineralization of gaseous formaldehyde on a novel self-supporting Cu_{2-x}Se/Cu₂O heterojunction photocatalyst under visible lights: A viable mesh for designing air purifier

Wei Liu ^{1,a}, Mengyi Shi ^{1,a}, Yingting Li ^b, Ziyi Wu ^a, Lixia Yang ^{a,*}, Shuqu Zhang ^{a,b}, Xiao Xiao ^a, Chengjin Liu ^a, Weili Dai ^{a,*}, Congjing Chen ^b, Xinman Tu ^a, Jianping Zou ^a, Xubiao Luo ^a

^a Key Laboratory of Jiangxi Province for Persistent Pollutants Control and Resources Recycle, Nanchang Hangkong University, Nanchang 330063, Jiangxi Province, China

^b School of art and design, Nanchang Hangkong University, Nanchang 330063, Jiangxi Province, China



ARTICLE INFO

Keywords:

Self-supporting
Cu_{2-x}Se/Cu₂O
Formaldehyde
Photocatalytic degradation
Indoor air

ABSTRACT

Reinforced adsorption enabled efficient degradation of formaldehyde was investigated with a unique flower-like Cu_{2-x}Se/Cu₂O heterojunction photocatalyst. Nonstoichiometric Cu_{2-x}Se crystals are grown from a pliable Cu mesh through a self-sacrifice template strategy. Sintering Cu_{2-x}Se in O₂/N₂ atmosphere enables the formation of Cu_{2-x}Se/Cu₂O heterojunction. The implantation of Cu₂O lowers the work function of Cu_{2-x}Se and boosts the gathering of electrons, qualifying the heterojunction as electron-rich area with those shared Cu atoms being active sites. Under illumination, abundant electrons on Cu_{2-x}Se/Cu₂O delocalize to attract formaldehyde molecules and convert them into semi-stable carbonates. Simultaneously, these electrons react with adsorbed oxygen to produce active •O₂. With a continuous-flow operation mode, 100% removal percentage and 99.5% CO₂ conversion rate are achieved when eliminating formaldehyde. By virtue of its integrity and pliability, the Cu mesh bearing Cu_{2-x}Se/Cu₂O can be applied in air purifier directly.

1. Introduction

The past few decades have witnessed a dramatic change in our life-style. Modern amenities undoubtedly make life much easier than before on many accounts and bring us into the era of the “Indoor Generation” at the same time. Many people on average spend more than 90% of their time indoors [1], for their concerns are laid on some kinds of screens encompassing computers, smartphones, and game consoles, etc. It was reported that each year, 5.5 million people worldwide die from diseases attributed to polluted indoor air [2]. Thereby, ensuring high indoor air quality is essential for human health, especially in the epidemic time. There are diverse pollutants in the air, which can be approximately classified as microorganisms, particulate matter, and volatile organic chemicals (VOCs) [3].

VOCs generally refers to the human-made chemicals that are used and produced in the manufacture of paints, pharmaceuticals, and

refrigerants, which have a high vapor pressure and low water solubility [3]. Formaldehyde, benzene, and toluene are top-ranked three VOCs that people are familiar with, for they are frequently reported in news and known as hazardous carcinogens [4]. Among them, formaldehyde is almost ubiquitous in atmospheric circumstances, it is a colorless chemical with a strong odor. Sources of indoor formaldehyde include pressed-wood, adhesives, fabrics and insulation materials, etc, which are necessary building materials for a new house. Besides, modern home furnishings and fuel-burning are other significant origins of indoor formaldehyde pollution [5]. Working or living in an environment with excess formaldehyde in a short period may cause the irritation of eye, nose, and throat, headaches. Long-term exposure to formaldehyde has been verified to be related to an increased threat of cancers like nasopharyngeal and oropharyngeal cancer, and lung cancers in humans. Therefore, various approaches have been developed to remove formaldehyde from the air (particularly that in the indoor environment) and

* Corresponding authors.

E-mail addresses: yangliax829@163.com (L. Yang), wldai81@126.com (W. Dai).

¹ Wei Liu and Mengyi Shi contribute equally to this work.

mitigate possible risks to human health [6,7].

Except for ventilation, strategies of eliminating formaldehyde indoor can be categorized into two groups: adsorption, and catalytic oxidation [8,9]. Adsorption contains physical adsorption and chemical adsorption. For instance, taking advantage of the high surface area of active carbon to remove indoor formaldehyde is assigned to physical adsorption [10]. Employing S or N doped porous carbon [11], or NaOH-modified ceramic honeycomb [12], to realize the reinforced immobilization of formaldehyde belongs to the chemical adsorption group. Nevertheless, adsorption is a process that gathers and holds formaldehyde molecules without changing their chemical structures, which can not get rid of the toxicity of formaldehyde. And removal performance is limited by the adsorption capacity of adsorbents. As a promising alternative, catalytic oxidation especially like thermal catalytic degradation [13], plasma technology [14,15] can transfer formaldehyde or chlorinated-VOCs in non-toxic carbon dioxide and water. Especially, those catalysis performing at room temperature points out practical and promising strategies for indoor air control, such as employing Co-contained catalysts [16,17], Mn-based catalysts [18,19] and photocatalysis with semiconductors [20] for degrading formaldehyde. Among above methods, photocatalysis is the most attractive, for its low-energy input and high efficacy under ambient conditions.

Diverse photocatalysts have been explored for oxidizing formaldehyde, including the classical TiO_2 [21], and its composites: $\text{TiO}_2/\text{diamomite}$ [22], $\text{TiO}_2/\text{Ti foil}$ [23], Pt/TiO_2 [24], $\text{TiO}_2@\text{NH}_2\text{-MIL-125}$ [25], $\text{g-C}_3\text{N}_4$ [26], zeolitic imidazolate framework-8 (ZIF-8) [27], etc. Outstanding efficiency in eliminating formaldehyde in bench scale can be devoted by the photocatalysts mentioned above. But as most of them are powdery, a filming process with polymer binders is usually required for constructing a photocatalytic reactor, which probably minimizes the catalyst's surface area. Moreover, it is difficult for gaseous molecules to disperse and contact the active sites buried in the pressed catalyst powders. Self-supporting photocatalysts rooted in a solid substrate are much more practical [28,29]. On account of the inherently anchoring force between photocatalyst and substrate, they can be directly assembled in a reactor or an appliance, maintaining their pristine morphology and activity. Therefore, developing a self-supporting catalyst featuring with large surface, high affinity towards target chemicals can meet the demand for fast mineralizing hazardous VOCs.

Cu_{2-x}Se is a typical p-type semiconductor with a narrow energy bandgap of about 1.5 eV, and x changes in the range of 0.15–0.2, which is reported to have a direct band gap of 2.2 eV and an indirect band gap of 1.4 eV for $x = 0.2$. Cu_{2-x}Se can present a superior capacity of photovoltaic conversion [30,31]. All sorts of applications like gas sensing [32], in vivo photoacoustic imaging [33], lithium-strorage [34], photocatalyst [35] and thermoelectric converters were conducted using Cu_{2-x}Se . Particularly, the crystal structures and components of Cu_{2-x}Se can be easily regulated by controlling the synthesis methods and conditions. It is really a diverse candidate for photocatalysis. Therefore, in this work, a novel three-dimensional (3D) flower-like $\text{Cu}_{2-x}\text{Se}/\text{Cu}_2\text{O}$ composite grown from a flexible Cu mesh was synthesized through a self-sacrifice template approach and subsequent heat treatment. Every Cu wire knitted in Cu mesh was enwrapped by $\text{Cu}_{2-x}\text{Se}/\text{Cu}_2\text{O}$ nano-flowers which regularly spread on the substrate, building up a light-sensitive photocatalytic interface with high porosity. Under irradiation, plentiful photoinduced electrons enriched the catalyst surface, for the p-p $\text{Cu}_{2-x}\text{Se}/\text{Cu}_2\text{O}$ heterojunction drive the electrons to move outwards. When the formaldehyde molecules were adsorbed on $\text{Cu}_{2-x}\text{Se}/\text{Cu}_2\text{O}$, the congregated-electrons helped to immobilize them through electron delocalization. Plus the impact of abundant oxygen vacancies induced by the implantation of Cu_2O in Cu_{2-x}Se crystals, formaldehyde can be rapidly decomposed in CO_2 and H_2O under visible lights. This study not only figures out the root causes of the superior performance from $\text{Cu}_{2-x}\text{Se}/\text{Cu}_2\text{O}$, but also delivers a practical photocatalyst for designing and manufacturing an advanced air purifier.

2. Experimental section

2.1. Chemicals and materials

Selenium (Se) powder, sodium hydrate (NaOH) and NaBH_4 were purchased from Guoyao Co. Ltd. China. All the chemicals were of analytical grade and used without further purification. Red copper (Cu, 99.8% in purity) mesh was purchased from An Ping Hangying wier mesh products Co.Ltd, which was cleaned to remove the surface grease with aceton, ethanol and water in sequence.

2.2. Synthesis of $\text{Cu}_{2-x}\text{Se}/\text{Cu}$ and $\text{Cu}_{2-x}\text{Se}/\text{Cu}_2\text{O}/\text{Cu}$ photocatalyst

3D flower-like Cu_{2-x}Se crystals were prepared through a self-sacrifice template method. In a representative procedure, 1.25 g of NaOH and 0.0709 g of NaBH_4 were dissolved in 50 ml of deionized water. Then, 0.075 g of Se powders were added in the basic solution. Heated the solution to 60 °C and continuously stirred it until all the solid Se powders turned dissolved. The Se-containing homogeneous solution was bubbled with N_2 for 5 min to drive the dissolved oxygen out after it was naturally cooled to room temperature. Afterwards, a piece of Cu mesh (15 cm² in size) was immersed in the solution for 2 h with the reactor sealed. During this process, Cu_{2-x}Se crystals were spontaneously grown from Cu mesh which worked as Cu origin and substrate.

When the reaction was finished, took out the Cu mesh and washed it with ethanol and water to remove the residual chemicals. After the $\text{Cu}_{2-x}\text{Se}/\text{Cu}$ was dried in the air, it was then sintered at 250 °C in an N_2 atmosphere with variable O_2 contents: 0%, 5%, 10% and 15% to synthesize $\text{Cu}_{2-x}\text{Se}/\text{Cu}_2\text{O}$ heterojunction on Cu mesh. The resulting catalysts were noted as Cu_{2-x}Se , $\text{Cu}_{2-x}\text{Se}/5\%$ O_2 , $\text{Cu}_{2-x}\text{Se}/10\%$ O_2 , $\text{Cu}_{2-x}\text{Se}/15\%$ O_2 when discussing their properties.

2.3. Characterization

Structural and morphological information of Cu_{2-x}Se and $\text{Cu}_{2-x}\text{Se}/\text{Cu}_2\text{O}$ crystals were obtained using a scanning electron microscope (SEM, Hitachi-SU1510) and transmission electron microscope (TEM, FEI Talos F200X). The crystal phase of those prepared catalysts was analyzed with X-ray diffractometer (XRD, Bruker, D8advance). UV-vis spectrophotometer (Hitachi, U-3900 H) was used to determine the light absorption capacity of Cu_{2-x}Se and $\text{Cu}_{2-x}\text{Se}/\text{Cu}_2\text{O}$ by presenting related diffuse reflectance spectra. The elemental composition of the catalyst surface was determined using X-ray photoelectron spectroscopy (XPS, Thermomal, ESCALAB 250). In addition, a fluorescence spectrophotometer (Excitation wavelength, 300 nm; Hitachi F4500) was employed to record the photoluminescence (PL) spectra of the semiconductor catalysts to evaluate the separation efficiency of photogenerated excitons. Electrochemical measurements about insistent photocurrents and electrochemical impedance spectroscopy were conducted with an electrochemical workstation (Chenhua Instrument Co., CHI 660D). Electron paramagnetic resonance (EPR) and electron spin resonance (ESR) spectra were collected with an electron paramagnetic resonance spectrometer (Bruker A300). Species adsorbed on the catalyst during formaldehyde degradation were identified by employing In Situ diffuse reflectance infrared Fourier transform spectroscopy (Nicolet IS50, Thermo fisher).

2.4. Photocatalytic degradation of formaldehyde

Visible-light triggered degradation of formaldehyde was performed in a self-developed quartz reactor (330 ml) which was connected to a gas chromatograph (Fuli, GC9720 PLUS, China) equipped with a flame ionization detector (FID). CO_2 can be detected by gas chromatography (GC) but formaldehyde can not. The standard curve of CO_2 for GC analysis is shown in Fig. S1, corresponding R^2 is about 0.9995. A Xe lamp (Perfect light, PLS-SXE300) was employed to supply the visible

light source with a 420 nm-cut filter and an IR-cut filter. The light resource intensity is measured by an optical power meter (CEL-NP2000-2), which is about 110 mW/cm². Before turning on the light, 0.051 μL liquid formaldehyde (1.08 g/ml, 40 wt%) was injected into the reactor with an ultra-micro sampling syringe (Capacity:0.5 μL) through a valve embedded in reactor cover. After the liquid formaldehyde evaporated completely, took out the syringe and closed the valve. The final formaldehyde concentration was calculated as 50 ppm. During photocatalysis, take CO₂ yield as an indicator to assess the catalytic efficiency of those photocatalysts, described in the equation below.

$$E = \frac{C_{CO_2}}{C_{HCHO}} \times 100\%$$

Where E represents the conversion efficiency, C_{CO₂} is the instant concentration of CO₂ produced, and C_{HCHO} is the initial concentration of formaldehyde. For the relative humidity (RH) under ambient condition is generally around 70% in Southeast China, the RH in the reactor was maintained at 70% throughout the experiment.

2.5. Computational methods

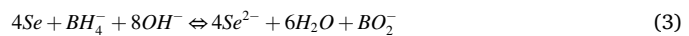
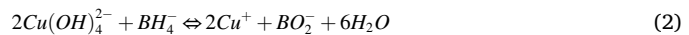
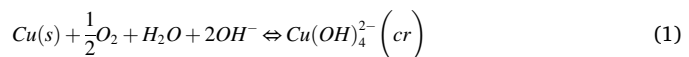
A Vienna Ab Initio Package (VASP) [36,37], was employed to conduct all the density functional theory (DFT) calculations within generalized gradient approximation (GGA) using the PBE formulation [38]. We chose the projected augmented wave (PAW) potentialsto describe the ionic cores and take valence electrons into account using a plane-wave basis set with a kinetic energy cutoff of 500 eV [39,40]. Partial occupancies of the Kohn–Sham orbitals were allowed using the Gaussian smearing method and a width of 0.05 eV. The electronic energy was considered self-consistent when the energy change was smaller than 10⁻⁵ eV. Geometry optimization was considered convergent when the force change was less than 0.04 eV/Å. Grimme's DFT-D3 methodology was used to describe the dispersion interactions [41]. In our calculation, the Free energy per cell (G/unit cell) can be obtained by G=E_{total}+E_{ZPE}T_S, where E_{total}, E_{ZPE}, and T_S represent the ground-state energy per unit cell, zero-point energies, and entropy terms, respectively, with the latter two taking vibration frequencies from DFT [42]. Finally, the reaction energies (G) of different intermediates are defined as ΔG=G_{product}-G_{reactant} (G_{product} is the energy of intermediates and G_{reactant} is the total energy of reactants).

3. Results and discussion

3.1. Synthesis and Characterization of Cu_{2-x}Se and Cu_{2-x}Se/Cu₂O on Cu mesh

3D flower-like Cu_{2-x}Se nanocrystals were spontaneously grown along every Cu wire surface by following a self-assembly style. Cu_{2-x}Se nanoplates are building blocks, they interconnect with each other to construct a porous interface (Fig. 1a-d). The SEM image of cross-section shows the thickness of Cu_{2-x}Se/Cu₂O layer is about 2.4 μm and a single nanosheet is 12. 5 nm thick (Fig. S2). It's true that the flower-like morphology will contribute to the high activity of Cu_{2-x}Se/Cu₂O. There are four essential advantages of nanoflowers. First, the high surface to volume ratio can enhance surface adsorption for accelerating the kinetics of reaction. Second, the three-dimensional structure supplies plenty of active sites due to the countless edges and corners. Third, nanoflowers demonstrate better charge transfer and carrier immobility caused by the interconnected nanoflakes. Fourth, the three-dimensional structure also helps to enhance the light-harvesting by reducing the reflection of lights. Furthermore, as the Cu_{2-x}Se is directly grown from the Cu substrate, the affinity between Cu_{2-x}Se layer and Cu is high, constructing an integrated, stable photocatalyst. Only intended destruction like vigorous bending or folding can damage the Cu_{2-x}Se layer.

The details in the growth procedure of Cu_{2-x}Se can be described as the following equations.



As Eq. (1) illustrates, in presence of O₂ and OH⁻, Cu can be oxidized and turn into amorphous Cu(OH)₄²⁻ spontaneously [28,29]. Then Cu (OH)₄²⁻ is reduced by BH₄⁻, generating Cu⁺ (Eq. 2). Since BH₄⁻ also reduces Se to Se²⁻ (Eq.3), Cu⁺, therefore, reacts with Se²⁻ (Eq.4). Because of the fast growth rate, the composite is not a perfect crystal, but

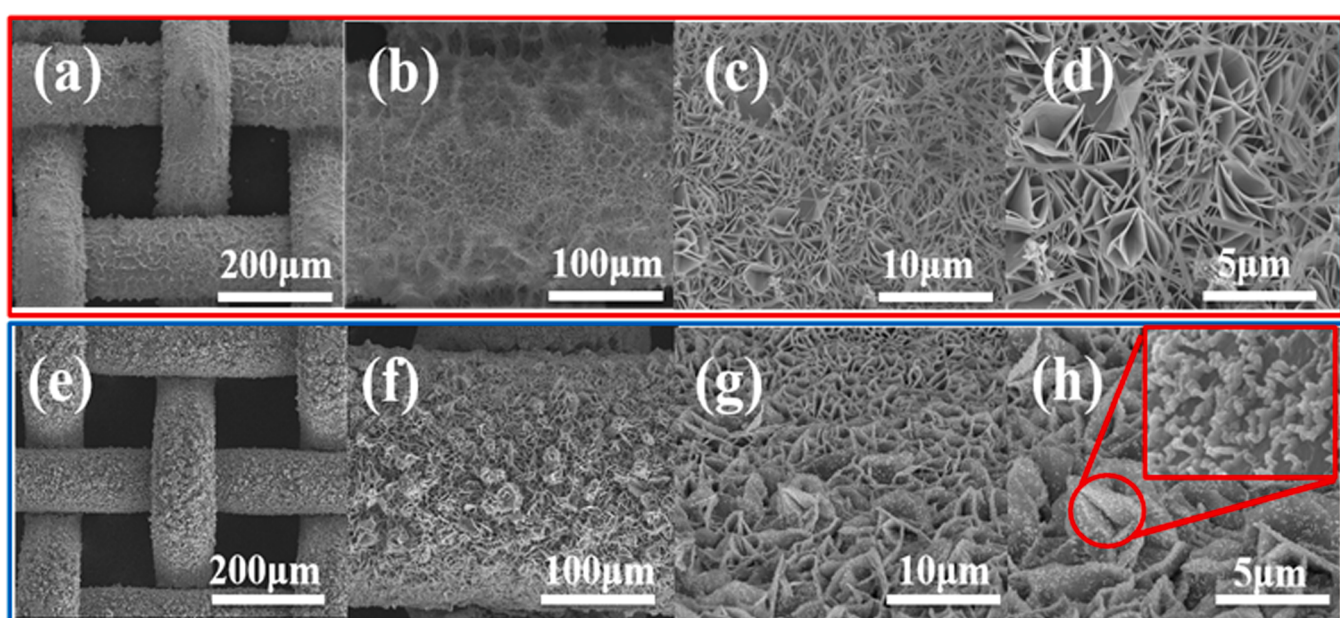


Fig. 1. (a)-(d) SEM images of Cu_{2-x}Se/Cu mesh with increased magnification; (e)-(h) SEM images of Cu_{2-x}Se/Cu₂O/Cu mesh with increased magnification.

nonstoichiometric Cu_{2-x}Se . After annealing in O_2/N_2 atmosphere at 250 °C, the resulting $\text{Cu}_{2-x}\text{Se}/\text{Cu}_2\text{O}$ crystals maintain the original morphology of Cu_{2-x}Se nanoflowers (Fig. 1e-h). Nevertheless, as shown in Fig. 1g and 1h, different from the smooth surface of pristine Cu_{2-x}Se , there are some nanoparticles loaded on $\text{Cu}_{2-x}\text{Se}/\text{Cu}_2\text{O}$ plates, which are probably SeO_2 particles. It is proposed that, driven by heat, O atom enters Cu_{2-x}Se lattices to form Cu-O bonds, and squeeze out Se atoms, which then react with O_2 and turn into SeO_2 . In addition, EDS spectrum of $\text{Cu}_{2-x}\text{Se}/\text{Cu}_2\text{O}$ is shown as Fig. S3, with elemental composition listed in Table S2. Except Cu, Se, and O, no residual chemical for synthesizing Cu_{2-x}Se was detected, indicating they will not influence the photocatalytic process.

The XRD patterns (Fig. 2a) of Cu_{2-x}Se and those $\text{Cu}_{2-x}\text{Se}/\text{Cu}_2\text{O}$ calcined in O_2/N_2 atmosphere with increased O_2 amounts show that the more O_2 molecules there, the higher content of Cu_2O in the composites. The pristine Cu_{2-x}Se is indexed to the face-centered cubic (fcc) phase (JCPDS 06-0680). And the $\text{Cu}_{2-x}\text{Se}/\text{Cu}_2\text{O}$ crystals exhibit the same characteristic peaks located at 26.75°, 44.50° and 52.91°, which correspond to the (111), (220), (311) planes of Cu_{2-x}Se . Besides, the specific peaks relating to Cu_2O (JCPDS 05-0667) are observable, sited at 36.41°, 42.29°, 52.45°, 61.34°, respectively. As Fig. 2b depicts, in comparison with the original Cu_{2-x}Se , the magnified diffraction peak at 26.75° assigned to (111) plane of Cu_{2-x}Se negatively shifts as the O_2 content in the tube furnace increased. Demonstrated as the proposed atomic models in Fig. 2c, Cu_2O and Cu_{2-x}Se lattices share two Cu atoms (marked by black rectangles), constructing a co-growth heterojunction. The implantation of Cu_2O in Cu_{2-x}Se nanoplates makes Cu_{2-x}Se lattices distorted and arises the expanded lattice spacing in the plane (111). In Fig. 2b, the original diffraction angle of Cu_{2-x}Se in the plane (111) remarkably shifts to small-angle direction.

Details in TEM analysis about Cu_{2-x}Se and those $\text{Cu}_{2-x}\text{Se}/\text{Cu}_2\text{O}$

confirm the above models. As shown in Fig. 3a and b, the pristine Cu_{2-x}Se nanoplates exhibit uniform lattice fringes along the (111) plane, corresponding fringe spacing is 0.33 nm (Fig. 3b). Regarding the $\text{Cu}_{2-x}\text{Se}/\text{Cu}_2\text{O}$ nanoplates, the magnified area marked in Fig. 3c exhibit the co-growth of Cu_{2-x}Se and Cu_2O . In Fig. 3d, besides the lattice fringes associated with Cu_{2-x}Se (111) planes, the lattice spacings of 0.24 nm and 0.21 nm correspond to (111) and (200) planes of Cu_2O , respectively. On the strength of in-situ substitution of Se with O, the original structure in Cu_{2-x}Se crystal lattices are deformed, which is presented as the bending Cu_{2-x}Se (111) planes near Cu_2O (Fig. 3e). In addition, demonstrated as Fig. 3f, zigzagged lattice fringes are captured as well, for some Cu atoms relocate to combine O atoms, resulting in the mismatch and lattice defects along Cu_{2-x}Se (111) planes.

Elemental mapping pictures of Cu, Se and O in Fig. S4 show that changes in O distribution on Cu_{2-x}Se and $\text{Cu}_{2-x}\text{Se}/\text{Cu}_2\text{O}$. Virtually, O atoms are detected on both of them, but its content in $\text{Cu}_{2-x}\text{Se}/\text{Cu}_2\text{O}$ is much higher than Cu_{2-x}Se , and the dispersion is more uniform. We attribute the O signal on pristine Cu_{2-x}Se to the adsorbed O_2 from the air, which can be evidenced by the following XPS analysis.

In Fig. 4a, only a single peak (531.5 eV) associated with adsorbed oxygen (O_{ads}) is demonstrated by Cu_{2-x}Se while three peaks indexed to O_{ads} at 531.2 eV, lattice oxygen (O_{latt}) at 529.6 eV and -OH from adsorbed water at 534.0 eV in sequence are observable on $\text{Cu}_{2-x}\text{Se}/\text{Cu}_2\text{O}$. The XPS spectra of O1s validate the chemical states of O, which is in line with the TEM analysis. As for Cu, after partial Se atoms are replaced by O atoms, the binding energies of 952.5 eV and 932.5 eV assigned to $\text{Cu} 2p_{1/2}$ and $\text{Cu} 2p_{3/2}$ positively shift to 953.6 eV and 933.5 eV, respectively (Fig. 4b) [43]. In addition, a new satellite peak at 942.9 eV assigned to Cu^{2+} is observed in $\text{Cu}_{2-x}\text{Se}/\text{Cu}_2\text{O}$ composite. The generation of Cu^{2+} is unavoidable during O_2 -contained heat treatment, but its content is low and the majority of Cu ions are Cu^+ . XPS spectra of

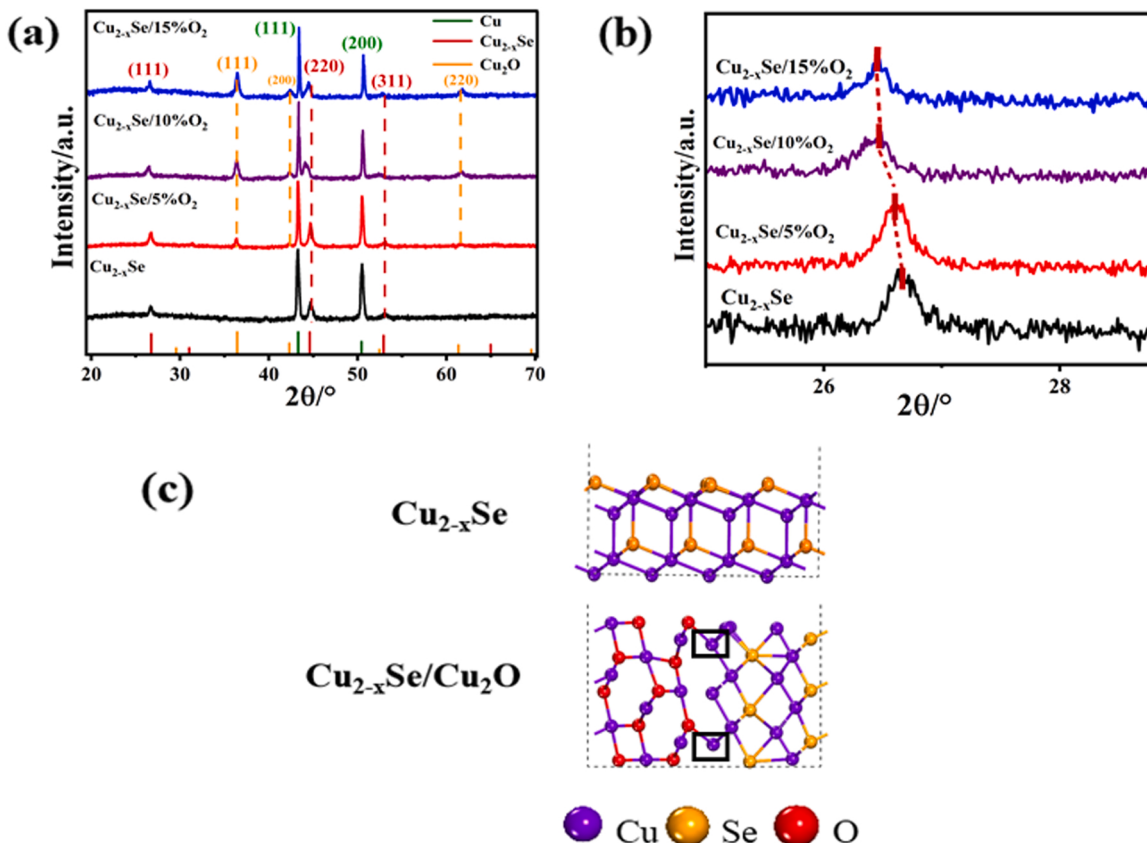


Fig. 2. (a) XRD pattern (Annealing at different oxygen concentrations), (b) Enlarged diffraction peak assigned to (111) plane of Cu_{2-x}Se , (c) Atomic model of Cu_{2-x}Se and $\text{Cu}_{2-x}\text{Se}/\text{Cu}_2\text{O}$ junction interface.

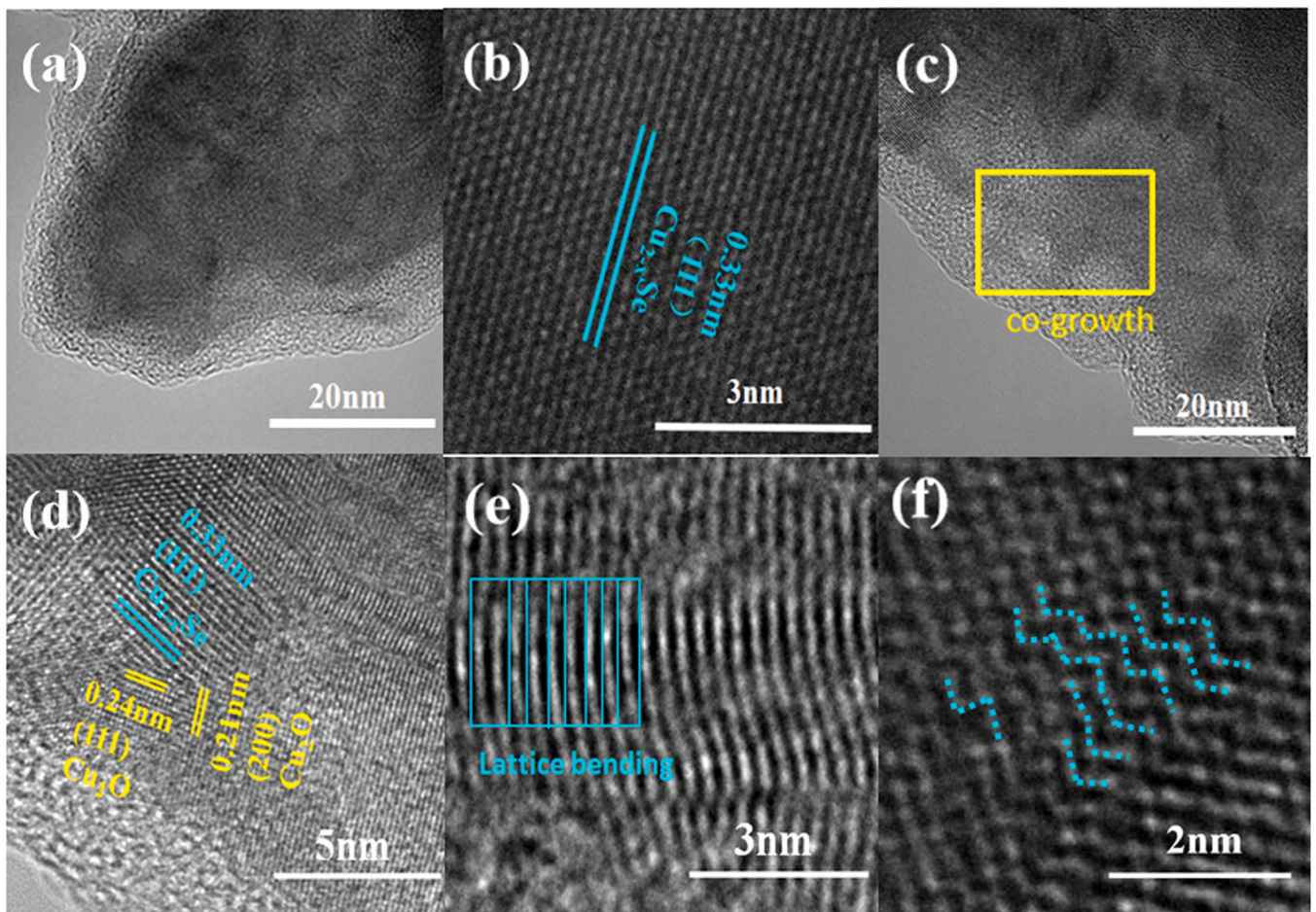


Fig. 3. Specific TEM analysis about Cu_{2-x}Se and Cu_{2-x}Se/Cu₂O. (a) low resolution TEM image of Cu_{2-x}Se, (b) enlarged lattice fringes of the area marked in (a); (c) TEM image of Cu_{2-x}Se/Cu₂O; (d), (e) and (f) corresponding defined analysis of the features at Cu_{2-x}Se/Cu₂O heterojunction interface.

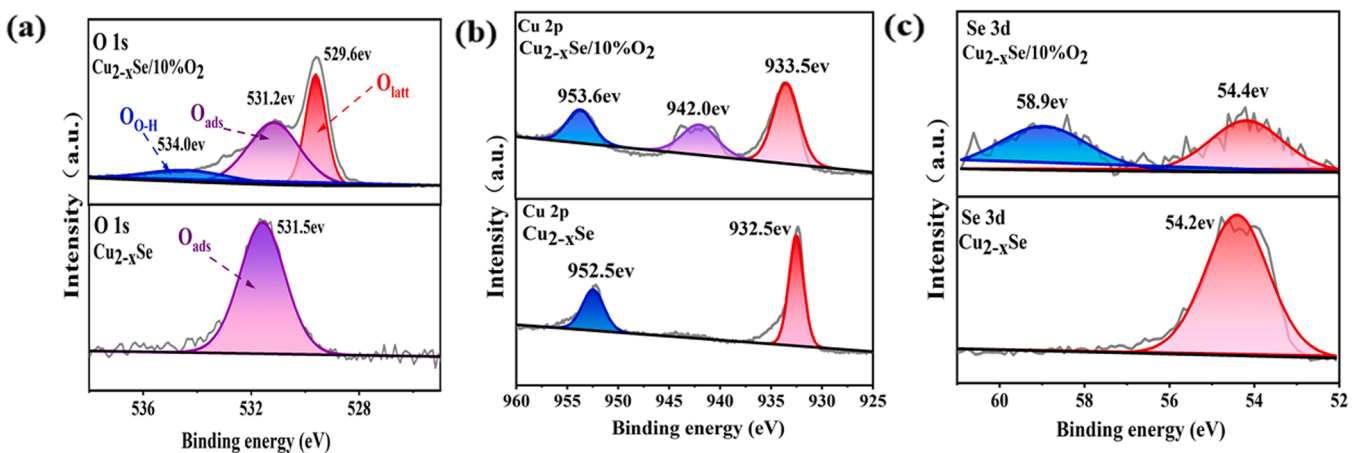


Fig. 4. High-resolution XPS spectra of (a) O1s, (b) Cu 2p, (c) Se 3d collected from pristine Cu_{2-x}Se and Cu_{2-x}Se/Cu₂O.

Se in Fig. 4c also change a lot. Compared with Cu_{2-x}Se, a new peak at 58.9 eV relating to Se⁴⁺ appears, which suggests that some Se²⁻ ions are oxidized by oxygen. Based on the aforementioned results, it comes out that the particles on Cu_{2-x}Se/Cu₂O surface are SeO₂. As SeO₂ is not a semiconductor, it does not contribute to the photocatalysis. However, if too many Se atoms are driven out by O and convert in SeO₂, the light harvest of Cu_{2-x}Se/Cu₂O will be restrained. Our research manifests that calcining Cu_{2-x}Se in N₂/O₂ (15%) leads to overloaded SeO₂ on

Cu_{2-x}Se/Cu₂O.

3.2. Photocatalytic degradation of formaldehyde using self-supporting Cu_{2-x}Se and Cu_{2-x}Se/Cu₂O

The implantation of Cu₂O in Cu_{2-x}Se builds a unique heterojunction photocatalyst that outperforms the pristine Cu_{2-x}Se in photoelectric conversion and electron transfer. Impact of Cu₂O on engineering the

photocatalytic activity of Cu_{2-x}Se in degrading formaldehyde was assessed by employing $\text{Cu}_{2-x}\text{Se}/\text{Cu}_2\text{O}$ meshes calcined in N_2/O_2 gas mixtures with increased O_2 volume ratios. The result about dark adsorption was provided as Fig. S5. In the absence of illumination, formaldehyde cannot be directly mineralized into CO_2 and H_2O .

Depicted as Fig. 5a, individual Cu_{2-x}Se is inferior to all the $\text{Cu}_{2-x}\text{Se}/\text{Cu}_2\text{O}$ composites. The optimal efficiency of eliminating HCHO is delivered by $\text{Cu}_{2-x}\text{Se}/10\% \text{O}_2$, which is almost two times that on Cu_{2-x}Se , illustrating that Cu_2O remarkably helps to accelerate photocatalysis. In the presence of $\text{Cu}_{2-x}\text{Se}/10\% \text{O}_2$, HCHO concentration in reactor rapidly goes down in the first 5 min and then declines slowly in the following time. Accordingly, the CO_2 yield sharply rises first, and then steadily grows until reaches its peak. When the photocatalysis is over, 100% removal percentage and 99.5% CO_2 conversion rate are obtained. Compared with $\text{Cu}_{2-x}\text{Se}/10\% \text{O}_2$, $\text{Cu}_{2-x}\text{Se}/15\% \text{O}_2$ demonstrates decreased catalytic efficiency because heating Cu_{2-x}Se in atmosphere with higher O_2 content results in over-doping of Cu_2O in Cu_{2-x}Se . As Se atoms are squeezed out by O and turn in SeO_2 , excess SeO_2 nanoparticles attached on Cu_{2-x}Se surface restrict the light adsorption and block active sites, leading to worse activity of $\text{Cu}_{2-x}\text{Se}/\text{Cu}_2\text{O}$. Therefore, the $\text{Cu}_{2-x}\text{Se}/10\% \text{O}_2$ is optimal.

As the kinetic curves in Fig. 5b show, the photocatalytic degradation of HCHO is a pseudo-1st-order reaction, it is an interface reaction controlled by the active radicals distributed on $\text{Cu}_{2-x}\text{Se}/10\% \text{O}_2$. In the following sections, all the $\text{Cu}_{2-x}\text{Se}/\text{Cu}_2\text{O}$ mentioned is the optimal one. Optical traits of $\text{Cu}_{2-x}\text{Se}/\text{Cu}_2\text{O}$ were exhibited by UV-vis diffuse reflectance spectra (DRS) and photoluminescence (PL) spectra. The harvest towards visible lights is remarkably strengthened because of the narrow-band-gap Cu_2O (Fig. S6a). The absorption peak centered at 650 nm is ascribed to the non-metallic plasma resonance [44–46], which originates from intrinsic copper atom defects and will benefit the production of hot electrons for catalysis. It's known that PL spectrum comes from the recombination of photoinduced excitons. As Fig. S6b show, with Cu_2O joined, the PL intensity of Cu_{2-x}Se is obviously declined, for the $\text{Cu}_{2-x}\text{Se}/\text{Cu}_2\text{O}$ heterojunction accelerates the separation of photo-induced e^-h^+ pairs. Consequently, the transient photocurrent recorded on $\text{Cu}_{2-x}\text{Se}/\text{Cu}_2\text{O}$ is dramatically enhanced, which is 5 times that on Cu_{2-x}Se (Fig. S6c).

Identification of active species that are responsible for HCHO degradation was carried out, with relating EPR spectra captured on Cu_{2-x}Se and $\text{Cu}_{2-x}\text{Se}/\text{Cu}_2\text{O}$ depicted in Fig. 6. Comparatively, the specific signal associated with $\bullet\text{O}_2$ on $\text{Cu}_{2-x}\text{Se}/\text{Cu}_2\text{O}$ is much tenser than on Cu_{2-x}Se whereas the increment concerning $\bullet\text{OH}$ signal is insignificant. That's because both Cu_{2-x}Se and Cu_2O are p-type semiconductors, the

built-in electric field drives the electrons to move outwardly and holes migrate internally. As a consequence, the increasement of $\bullet\text{O}_2$ yield is more notable than that of $\bullet\text{OH}$ yield. Since $\bullet\text{O}_2$ comes from the combination between O_2 and those photogenerated electrons, the strengthened $\bullet\text{O}_2$ signal clarifies that $\text{Cu}_{2-x}\text{Se}/\text{Cu}_2\text{O}$ has superior capacity in adsorbing and activating O_2 from the air than Cu_{2-x}Se . Furthermore, as depicted in Fig. 6c, oxygen vacancies (OVs) were detected on $\text{Cu}_{2-x}\text{Se}/\text{Cu}_2\text{O}$ as well, which are the point defects in Cu_2O . Therefore, besides the heterojunctions, OVs also contribute to the generation of $\bullet\text{O}_2$ owing to their inherent feature of adsorbing O_2 from the air [47–49].

Degradation of HCHO was performed under the conditions with variable O_2 content to confirm its influence on $\text{Cu}_{2-x}\text{Se}/\text{Cu}_2\text{O}$'s activity. Four contents were studied: 10%, 21% (content in natural air), 30%, 40%. As shown in Fig. S7a, the degradation rate is accelerated as increased O_2 contents, Reaction rate constant K increased from 0.195 at 10% O_2 to 0.204 at 21% O_2 . After that, the enhancement is not notable when O_2 content is 30% and 40%, for the active sites are saturated with O_2 . Moreover, the stable efficiency in successive 10 runs (Fig. S7c) using a $\text{Cu}_{2-x}\text{Se}/\text{Cu}_2\text{O}$ mesh confirms the durability, which is only declined by 4.2% in the 10th run compared with the 1st run. Resultantly, in view of the outstanding performance in eliminating HCHO under ambient conditions, $\text{Cu}_{2-x}\text{Se}/\text{Cu}_2\text{O}$ is practical, efficient, and promising in the manufacture of air purifiers. The influence of humidity on the degradation efficiency of formaldehyde by $\text{Cu}_{2-x}\text{Se}/\text{Cu}_2\text{O}$ catalysts was also studied. Within a common indoor humidity range (50%–80%), no significant changes are observable, as illustrated in Fig. S8. All the formaldehyde can be oxidized in CO_2 and H_2O in 30 min. That's because the major free carriers on $\text{Cu}_{2-x}\text{Se}/\text{Cu}_2\text{O}$ are electrons, which boost the generation of countless $\bullet\text{O}_2$. And the $\bullet\text{O}_2$ is responsible for the degradation of formaldehyde. As for $\bullet\text{OH}$, its amount is tiny, for the low potential of VB in Cu_{2-x}Se and Cu_2O . Consequently, the effect from humidity is not significant.

Adsorption behavior and transformation of HCHO molecules and relating intermediates generated from photocatalysis were recognized using in situ DRIFTS (In Situ diffuse reflectance infrared Fourier transform spectroscopy). Depicted as Fig. 7a, some HCHO molecules can be immediately uptaken by $\text{Cu}_{2-x}\text{Se}/\text{Cu}_2\text{O}$ and transformed into carbonate species centered at 1260, 1450, 1500 and 1650 cm^{-1} , and formate species located at 1590, 1820, 2970 cm^{-1} , which are all intermediates before HCHO completely mineralized [50,51]. Different from the catalysts reported in past work [52], that transformation occurs in absence of light irradiation, and the intensity of these species grows with adsorption time, which manifests that HCHO can be partially oxidized by the stabilized O_2 on $\text{Cu}_{2-x}\text{Se}/\text{Cu}_2\text{O}$ under ambient conditions. After

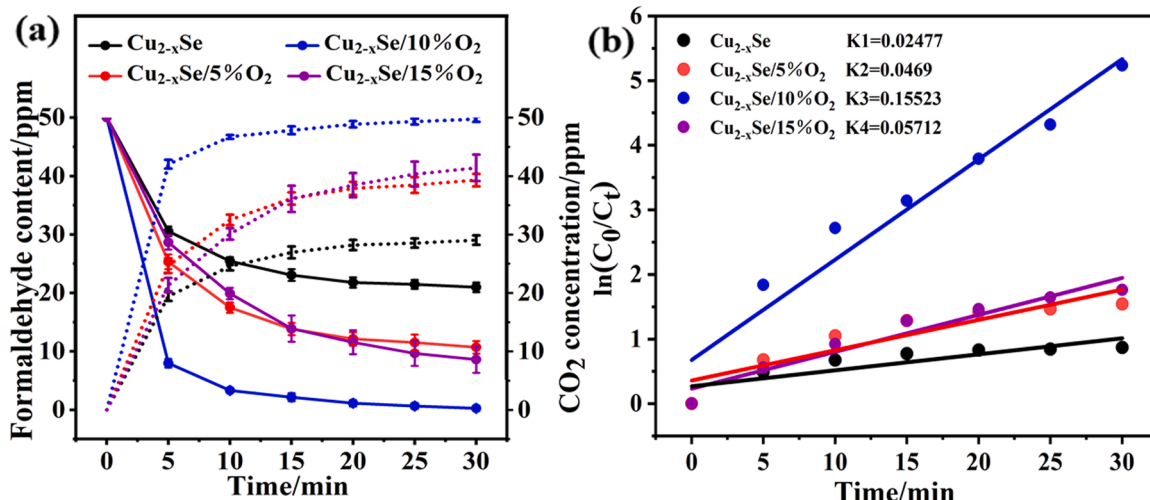


Fig. 5. (a) Residual formaldehyde and CO_2 yields over degradation duration with Cu_{2-x}Se and $\text{Cu}_{2-x}\text{Se}/\text{Cu}_2\text{O}$ meshes (b) corresponding kinetic analysis of formaldehyde degradation.

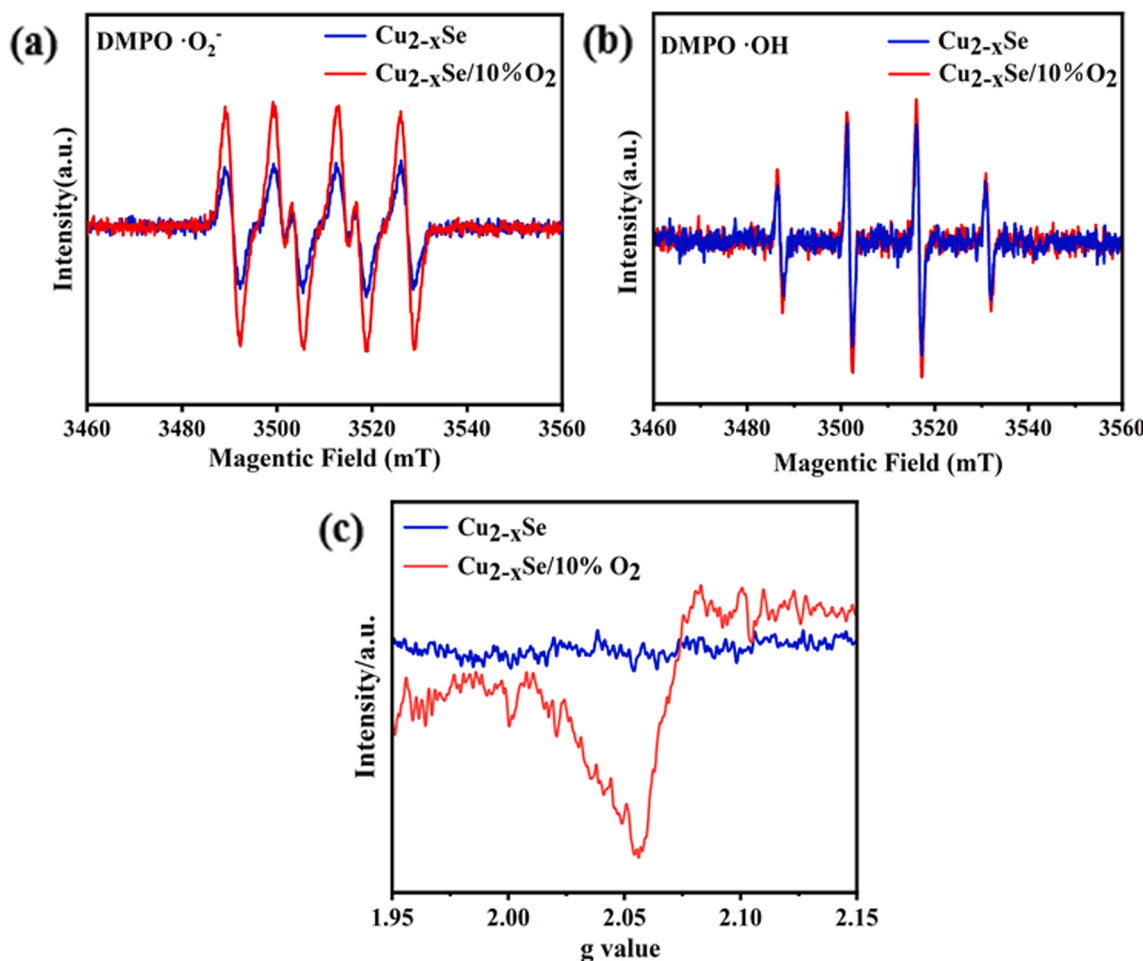


Fig. 6. ESR spectra of (a) $\cdot\text{O}_2^-$ and (b) $\cdot\text{OH}$ generated on Cu_{2-x}Se and $\text{Cu}_{2-x}\text{Se}/10\% \text{O}_2$. (c) EPR spectra of oxygen vacancies collected over Cu_{2-x}Se and $\text{Cu}_{2-x}\text{Se}/\text{Cu}_2\text{O}$.

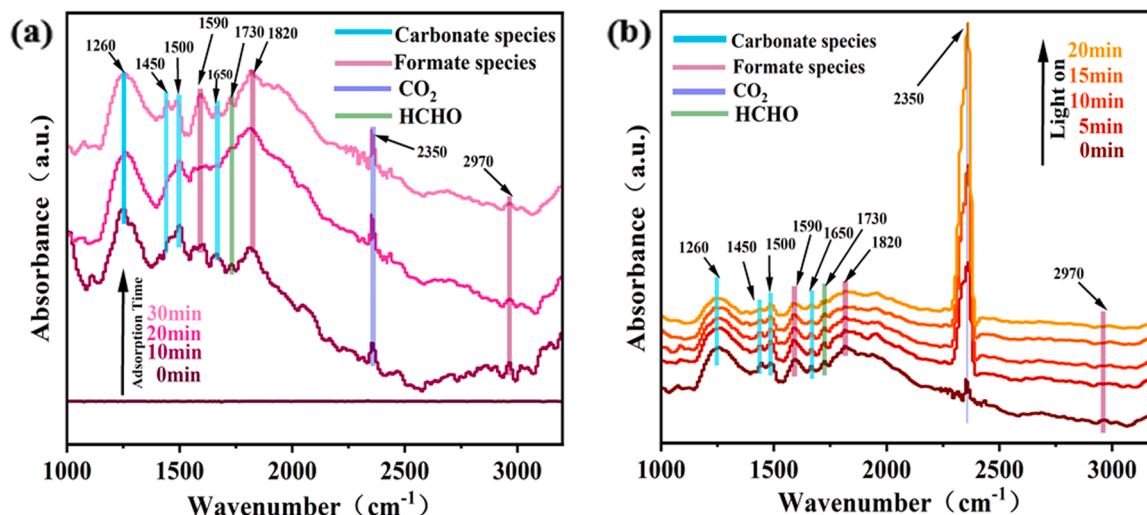


Fig. 7. In situ DRIFTS spectra of (a) HCHO adsorbed on $\text{Cu}_{2-x}\text{Se}/\text{Cu}_2\text{O}$, and (b) intermediates over $\text{Cu}_{2-x}\text{Se}/\text{Cu}_2\text{O}$ under visible lights. (Conditions: 50 ppm of HCHO, 10% O_2/He ; total flow rate, $100 \text{ cm}^3 \cdot \text{min}^{-1}$).

the light is turned on, the intensity of all the intermediates falls accompanied by the rapid growth of CO_2 , depicted as the specific peaks located at 2350 cm^{-1} in Fig. 7b. At the end of catalysis, HCHO molecules can be utterly oxidized in CO_2 and H_2O without posing any health risk.

The results in Fig. 7 manifest the exceptional capabilities of $\text{Cu}_{2-x}\text{Se}/\text{Cu}_2\text{O}$ in adsorbing, activating, and degrading HCHO.

3.3. Calculation analysis about electron transfer in $\text{Cu}_{2-x}\text{Se}/\text{Cu}_2\text{O}$ and involved photocatalytic mechanism

DOS figure of $\text{Cu}_{2-x}\text{Se}/\text{Cu}_2\text{O}$ in Fig. 8a depicts a notably enhanced DOS at valence band maximum (VBM) in comparison with the pristine Cu_{2-x}Se , indicating there are many more free electrons and verifying the positive effect of Cu_2O formation. Namely, after the heterojunction is formed, the O atom supplies atomic orbitals to accommodate electrons, contributing to building continuous molecules orbitals and facilitating the fast electron migration between Cu_2O and Cu_{2-x}Se . Comparing the electronic construction of Cu_{2-x}Se and $\text{Cu}_{2-x}\text{Se}/\text{Cu}_2\text{O}$ further discloses the reassembly and localization of electrons on the heterojunction interface. Displayed as the charge density differences in Fig. 8b, the valences electrons in individual Cu_{2-x}Se fill Se 4p and Cu 3d orbitals [53], exhibited as the yellow regions. After the heterojunction is formed, the electron clouds around Se atoms move towards Cu atoms. Meanwhile, the electrons circulating Cu_2O lattice also migrate towards Cu_{2-x}Se , giving out a trend of congregating along the joint (marked by the yellow round shape), which can be backed by the calculated work functions of Cu_{2-x}Se and $\text{Cu}_{2-x}\text{Se}/\text{Cu}_2\text{O}$ (Fig. S9). Work function represents the energy needed for electrons fleeing from a lattice's inner space to its surface. Generally, the lower the work function, the freer the electrons. The work function on Cu_{2-x}Se is 4.89 eV, and that on $\text{Cu}_{2-x}\text{Se}/\text{Cu}_2\text{O}$ is 4.81 eV, decreased by 0.08 eV. Cu_2O has a lower work function than Cu_{2-x}Se . As a result, the electrons on Cu_2O can be attracted and flow towards Cu_{2-x}Se . The gathering of electrons qualifies the joint between $\text{Cu}_{2-x}\text{Se}/\text{Cu}_2\text{O}$ to be an electron-rich area with those Cu atoms shared by Cu_{2-x}Se and Cu_2O lattices as active sites [54].

By analyzing the energy band gaps of individual Cu_{2-x}Se and Cu_2O , the carrier transfer behavior in $\text{Cu}_{2-x}\text{Se}/\text{Cu}_2\text{O}$ heterojunction is illustrated. As for individual Cu_2O , it was obtained by calcining Cu_{2-x}Se at 250 °C for 3 h in 30% O_2/N_2 atmosphere, the long process filled with abundant oxygen enable the complete conversion from Cu_{2-x}Se to Cu_2O . Depicted as Fig. 9a, band gap energies of individual

Cu_{2-x}Se and Cu_2O were estimated from a plot of $(\alpha h\nu)^2$ versus photo energy ($h\nu$) based on the UV-vis spectra in Fig. S6a, which is 1.61 eV for $\text{Cu}_{2-x}\text{Se}/\text{Cu}$, and 2.39 eV for Cu_2O . VB-XPS spectra in Fig. 9b depict the valence band (VB) potential of Cu_{2-x}Se is 1.17 V, that of Cu_2O is 1.71 V. Based on Fig. 9a and b, the conduction band (CB) potential of Cu_{2-x}Se is -0.44 V, and that of Cu_2O is -0.68 V. Since both Cu_{2-x}Se and Cu_2O are p-type semiconductor, they build a p-p heterojunction and the construction type is straddling, the most common sort among the three types of possible heterojunctions, Type I (straddling), Type II (staggered), and Type III (broken gap) [55]. In the light of the significant enhancement in mineralizing formaldehyde after $\text{Cu}_{2-x}\text{Se}/\text{Cu}_2\text{O}$ formed and the ELF results in Fig. 8, an energy band diagram illustrating the carrier transfer behavior in $\text{Cu}_{2-x}\text{Se}/\text{Cu}_2\text{O}$ is proposed.

As shown in Fig. 9c, the band gap of Cu_{2-x}Se is completely contained in the bandgap of Cu_2O . When the junction constructed, carriers will flow across the junction, building space charges until the Fermi energy is the same everywhere in the catalyst. Therefore, the band of Cu_2O bends downwards, and that of Cu_{2-x}Se bends upwards, leading to the photo-generated electrons in Cu_2O CB migrating towards Cu_{2-x}Se CB. Meanwhile, VB cusp and notch are formed on the joint interface between Cu_{2-x}Se and Cu_2O [56]. The potential barrier formed by the spike prevents holes transferring (named as effect of charge carrier confinement) [57], curbs the recombination of electron-hole pairs on the same side, facilitating the electrons' congregation on $\text{Cu}_{2-x}\text{Se}/\text{Cu}_2\text{O}$ interface. In Fig. 9d, the surface photovoltage detected on $\text{Cu}_{2-x}\text{Se}/\text{Cu}_2\text{O}$ is 1460 μV , almost twice that on Cu_{2-x}Se , validating $\text{Cu}_{2-x}\text{Se}/\text{Cu}_2\text{O}$ is able to deliver many more electrons than Cu_{2-x}Se . As the potential for electrons change the adsorbed O_2 into $\bullet\text{O}_2$ is -0.33 V, the electrons accumulated in Cu_{2-x}Se CB (-0.44 V) can render the formation of $\bullet\text{O}_2$.

Firm adsorption of target chemicals on catalyst surface is the first and vital step to boost an efficient gas-solid reaction, which determines the flowing procedures like mass transfer and catalysis reaction. Adsorption energies of HCHO , O_2 , H_2O on Cu_{2-x}Se and $\text{Cu}_{2-x}\text{Se}/\text{Cu}_2\text{O}$ were calculated with the deformation electron densities of them, as shown in

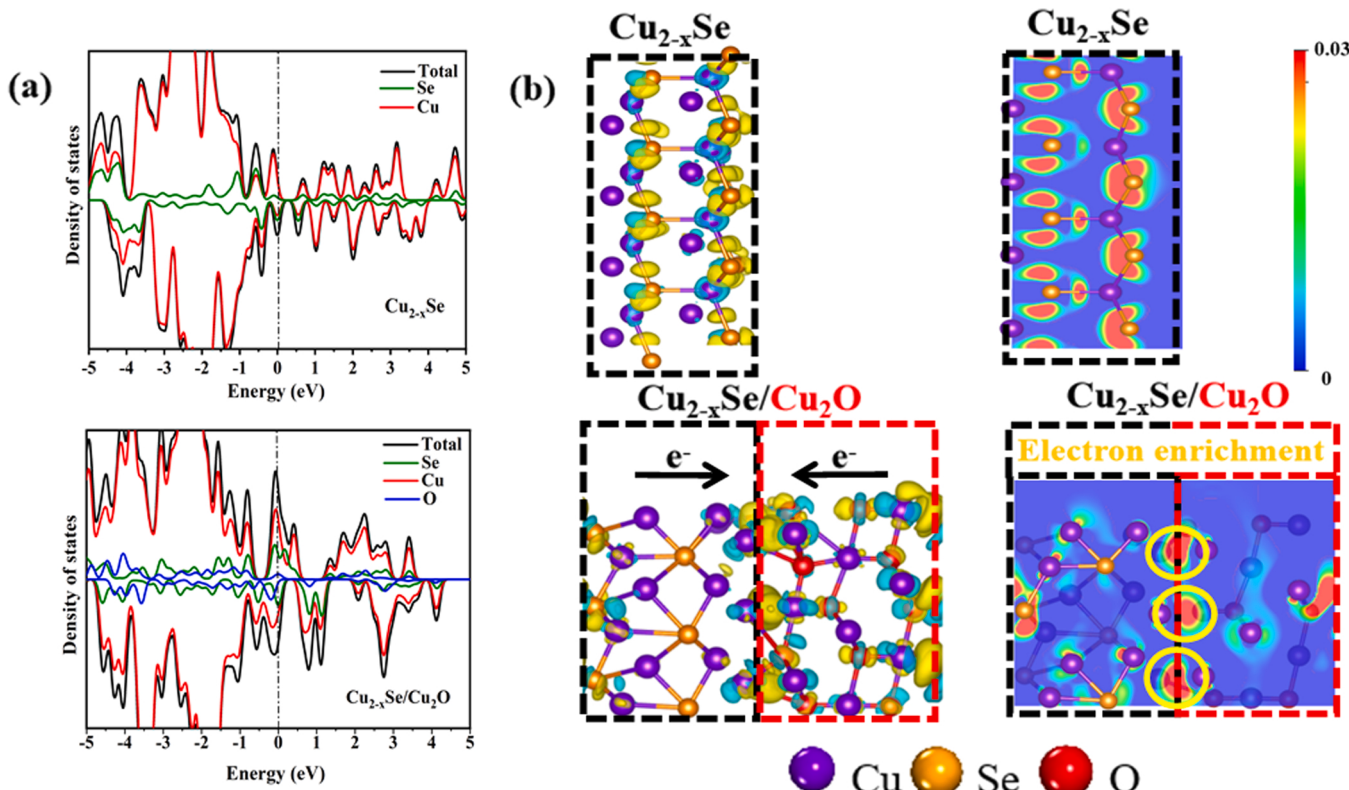


Fig. 8. (a) Density of state (DOS) and (b) Charge density difference, and electronic localization function (ELF) of Cu_{2-x}Se , $\text{Cu}_{2-x}\text{Se}/\text{Cu}_2\text{O}$.

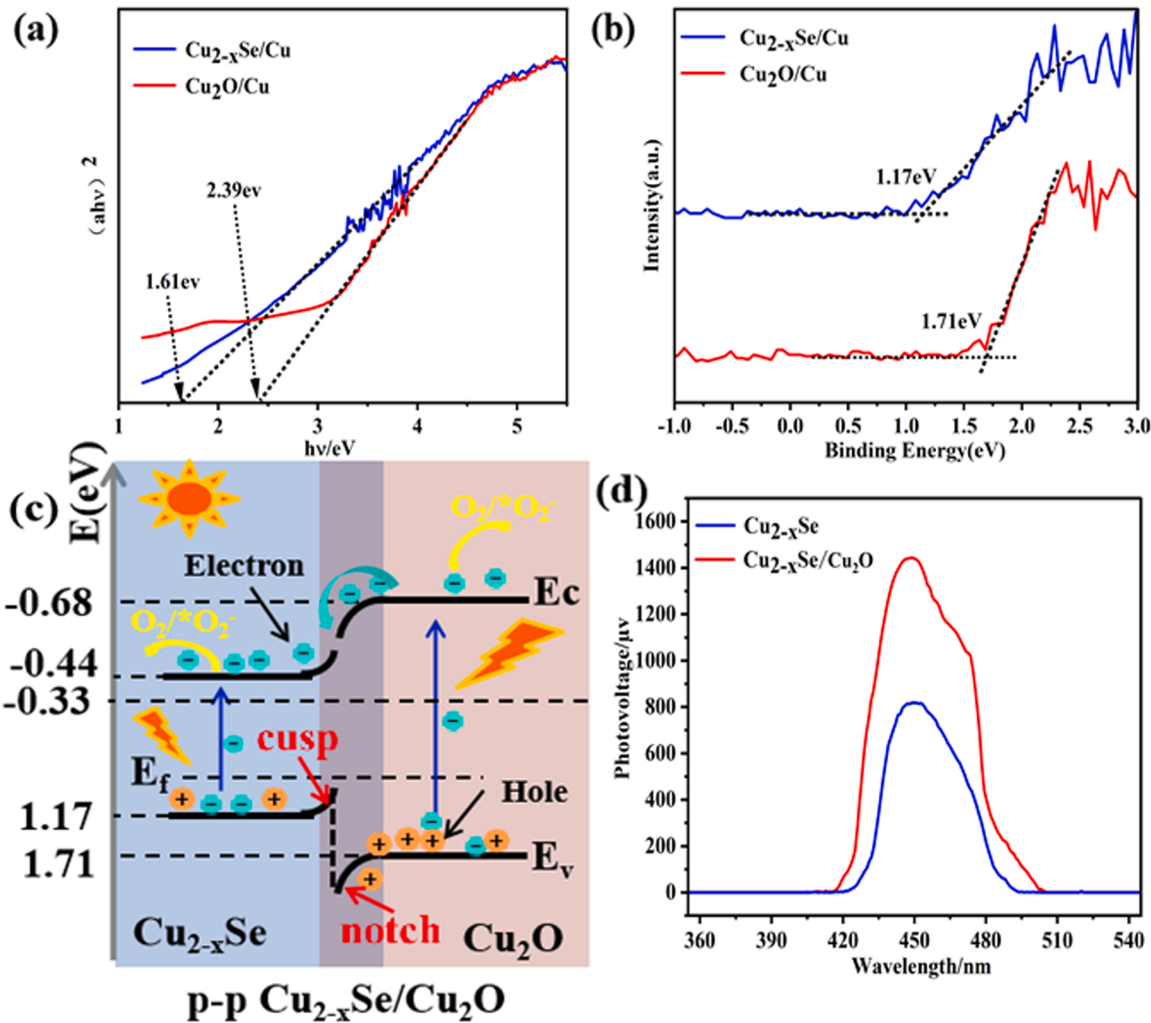


Fig. 9. (a) Energy band gap, (b) VB-XPS spectra of Cu_{2-x}Se and Cu_2O , (c) Energy band diagram and electron transfer process in the p-p $\text{Cu}_{2-x}\text{Se}/\text{Cu}_2\text{O}$ heterojunction. (d) SPV spectra of Cu_{2-x}Se and $\text{Cu}_{2-x}\text{Se}/\text{Cu}_2\text{O}$.

Fig. 10. Blue regions are electron-deficient, yellow regions stand for electron-abundant. Both Cu_{2-x}Se and $\text{Cu}_{2-x}\text{Se}/\text{Cu}_2\text{O}$ provide Cu atoms as anchorages to stabilize O₂, H₂O and HCHO, but $\text{Cu}_{2-x}\text{Se}/\text{Cu}_2\text{O}$ demonstrates higher affinity toward O₂, H₂O and HCHO than the pristine Cu_{2-x}Se . The adsorption energy for HCHO is -1.336 eV on pristine Cu_{2-x}Se and -1.587 eV on $\text{Cu}_{2-x}\text{Se}/\text{Cu}_2\text{O}$. Especially, the adsorption energy of O₂ molecules on $\text{Cu}_{2-x}\text{Se}/\text{Cu}_2\text{O}$ is -0.971 eV, two times that on Cu_{2-x}Se , -0.475 eV. Furthermore, compared with those adsorbed on Cu_{2-x}Se , HCHO, O₂, and H₂O on the heterojunction interface in $\text{Cu}_{2-x}\text{Se}/\text{Cu}_2\text{O}$ have more yellow regions, indicating those molecules are notably activated by the electrons from $\text{Cu}_{2-x}\text{Se}/\text{Cu}_2\text{O}$. There are electron streams and affirm bonds formed between gaseous molecules and the heterojunction photocatalysts. Moreover, as Fig. S10 shows, the contact angle of water determined on Cu_{2-x}Se is 82.1°, which is 45.0° on $\text{Cu}_{2-x}\text{Se}/\text{Cu}_2\text{O}$, evidencing the polarity of catalytic interface is enhanced due to doping of Cu_2O in Cu_{2-x}Se . And the improved polarity facilitates the adsorption of target molecules. The reinforced adsorption makes it achievable to activate HCHO, O₂, and H₂O and then scales back the reaction barrier. Namely, $\text{Cu}_{2-x}\text{Se}/\text{Cu}_2\text{O}$ is certain to produce many more active oxygen species, more unstable HCHO, accounting for the fast and efficient mineralization of HCHO.

The above analysis is further validated by Fig. 11a. As shown, all the calculated free energies for those intermediates involved in the HCHO degradation process with $\text{Cu}_{2-x}\text{Se}/\text{Cu}_2\text{O}$ are lower than those with Cu_{2-x}Se . In particular, the free energy for activating O₂ on Cu_{2-x}Se is

-0.455 eV, which is decreased to -1.396 eV on $\text{Cu}_{2-x}\text{Se}/\text{Cu}_2\text{O}$, minimized by 0.941 eV. This notable fall suggests that $\text{Cu}_{2-x}\text{Se}/\text{Cu}_2\text{O}$ heterojunction has superior capability in supplying thermodynamic fueling power for creating radicals to oxidize HCHO than individual Cu_{2-x}Se .

Enriched with abundant electrons and adsorbed O₂, active oxygen species governs the degradation pathway of HCHO (Fig. 11b). When both O₂ and HCHO are adsorbed on the $\text{Cu}_{2-x}\text{Se}/\text{Cu}_2\text{O}$, they are anchored and activated by the high-electron-density interface. O₂ turns in •O₂ and O^{*}, which are labeled as O^{*}. The carbon atoms in HCHO is attacked by O^{*} and accept the O atom accompanied with detaching an unsaturated hydrogen atom. This free H^{*} combines the chem-absorbed O₂ and becomes •OH [58]. Although the VB potentials of Cu_{2-x}Se and Cu_2O are less than 1.99 V($\phi_{\text{OH}/\text{H}_2\text{O}}$), the holes in Cu_{2-x}Se and Cu_2O are not capable of directly oxidizing the adsorbed H₂O to •OH, the abundant O^{*} originating from •O₂ can fuel the production of •OH (Fig. 11b). With the above reactions going on, more and more HCHO molecules transform in carbonate species and then decompose in CO₂ and H₂O.

A continuous-flow system (Fig. S11) consisting of a light source, peristaltic pump, the gas bag was designed to evaluate the practicability of $\text{Cu}_{2-x}\text{Se}/\text{Cu}_2\text{O}$ mesh. 8 L of 10 ppm HCHO can be completely mineralized in CO₂ and H₂O in 10 min (Fig. 12a), the elimination efficiency is 100%. With HCHO concentration increased, the $\text{Cu}_{2-x}\text{Se}/\text{Cu}_2\text{O}$ maintains its high efficacy even at 50 ppm HCHO, evidencing its promising prospect in practice. The long-term stability is specified as

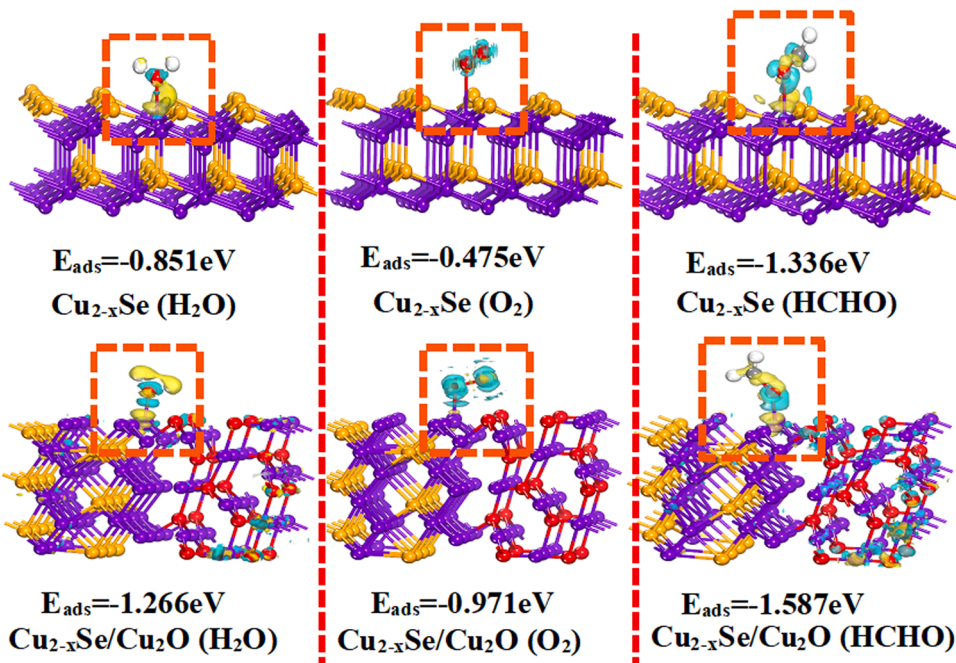


Fig. 10. Most stable configuration of HCHO, O₂, H₂O molecules adsorbed on Cu_{2-x}Se and Cu_{2-x}Se/Cu₂O and related adsorption energy (E_{ads}).

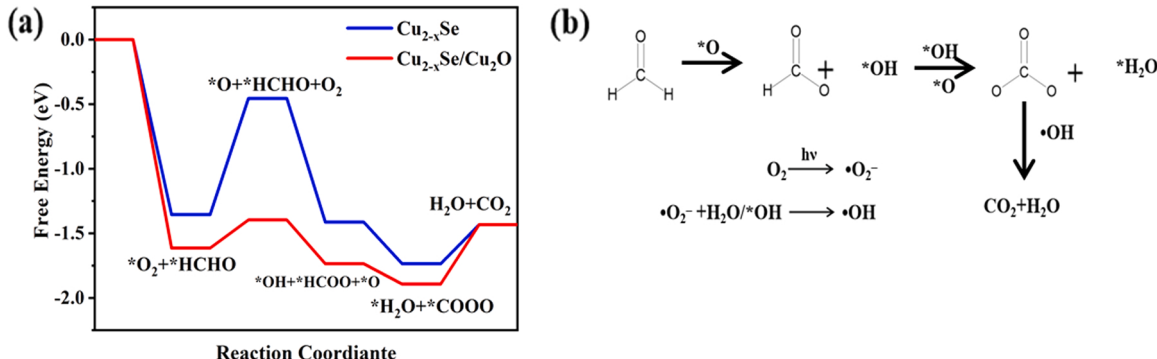


Fig. 11. (a) Calculated free energies for the conversion of O₂, H₂O and HCHO in intermediates, (b) proposed pathway for HCHO degradation.

Fig. 12b, which can evaluate its effective lifetime. The reactor worked continuously for 8 h. As the Cu_{2-x}Se/Cu₂O mesh can degrade 50 ppm HCHO (8 L) in 40 min, the air in the reactor was renewed with HCHO every 40 min. Simultaneously, the CO₂ yield was monitored online using a GC. As shown, the CO₂ content in the reactor grows steadily by exhibiting a stairs-shaped growing tendency. The degradation percentage in 12th run is about 90%, which manifests the outstanding efficacy and stability of Cu_{2-x}Se/Cu₂O mesh. In **Fig. 12c**, the scheme displays that the Cu_{2-x}Se/Cu₂O mesh is like a barrier to keep the indoor air from being polluted. Illuminated by lights, reactive oxygen species like ·O₂ and O⁻ are generated from Cu_{2-x}Se/Cu₂O mesh and distributed on it. As HCHO encounters O^{*}, it transforms in CO₂ and H₂O.

3.4. Design of an air purifier with tube-in-tube construction

With the growing awareness of air quality, it has become common to have an air purifier at home to protect people from living in polluted air. The design of photocatalytic air purifier is based on the aerodynamic theoretical model [59]. A fan is set in the purifier bottom to ensure the flow of indoor air. The purifier is 560 mm high and 250 mm in diameter, which is suitable for a room whose size is at least 60 cubic meters. As a self-supporting photocatalyst (the digital picture in **Scheme 1a**), the

Cu_{2-x}Se/Cu₂O/Cu mesh is flexible and conductive, which can be assembled in the air purifier directly with streamlined design and manufacturing process. A column shape air purifier (**Scheme 1a**) was designed with six (or more than six) small tubes with one open top. In those tubes are rolled Cu_{2-x}Se/Cu₂O/Cu mesh, demonstrating a unique tube-in-tube construction. This design generates circumfluent air flow inside the Cu_{2-x}Se/Cu₂O/Cu equipped tube (**Scheme 1c**). When the air enters the purifier from the bottom, suspended particles in the air are removed using a high efficiency particulate air filter (9 HEPA) which is equipped behind the fan. As the air flow approaches the baffle-3, it turns back and flows around the Cu_{2-x}Se/Cu₂O/Cu tube, creating a circling airstream and prolonging the contact time between air and Cu_{2-x}Se/Cu₂O/Cu mesh. After formaldehyde turns in CO₂ and H₂O under the irradiation from those built-in lamps-4, the purified air flows outwards through the outlet at the top.

Except for the photocatalytic performance in removing VOCs, this design is optimal to filter particles with variable density by creating air circulation in the room [60]. The manufacture of air purifier is still on the way, for translating good intentions into reality really takes a long time. We think this is an Eco-design because it integrates multifunction of environmental considerations, which can meet the demands for healthy air in the room.

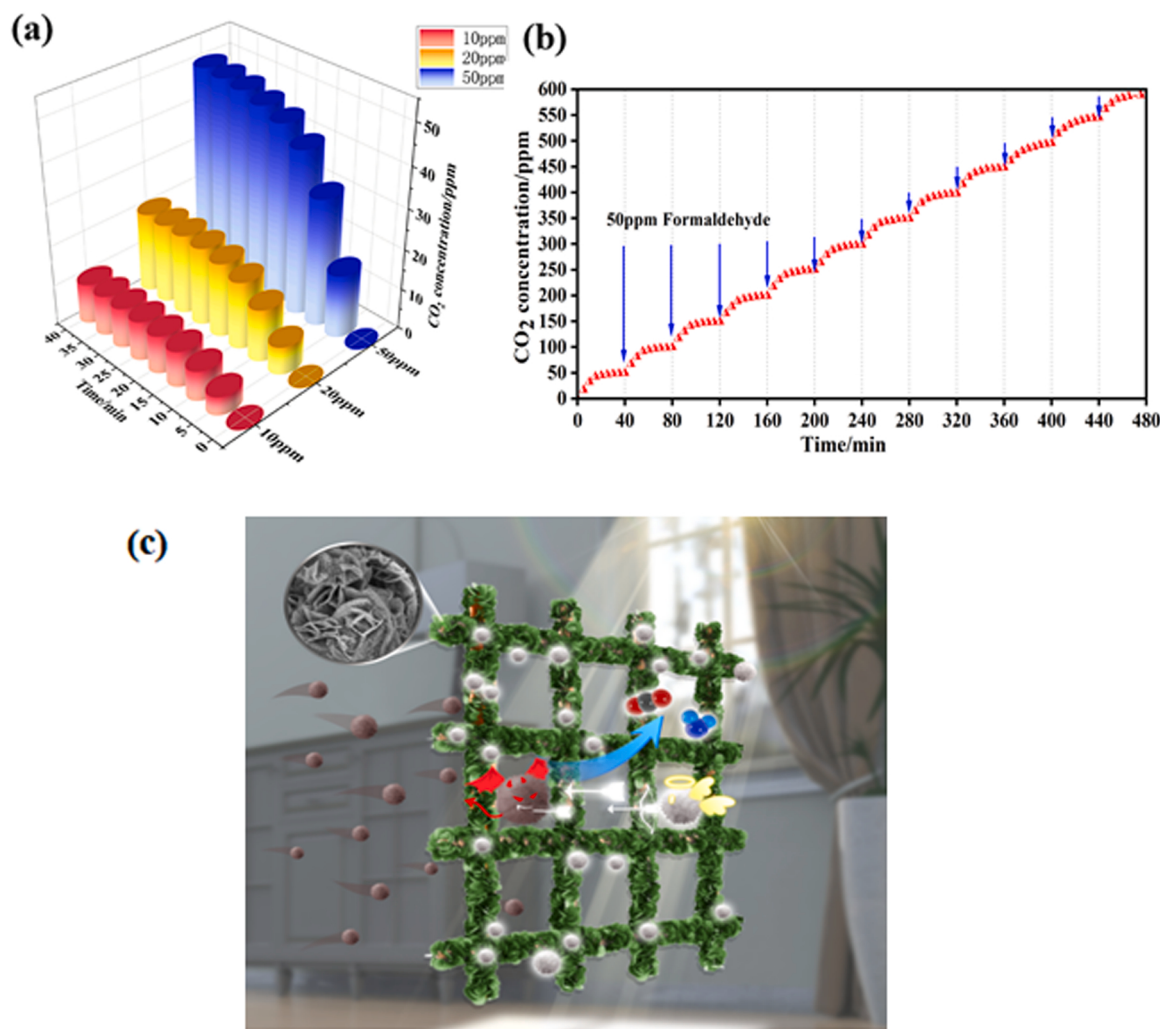
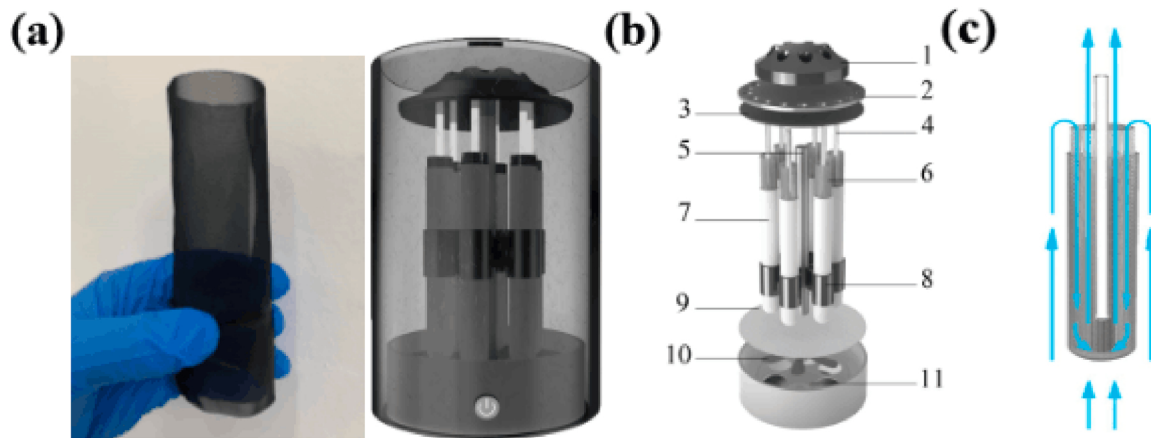


Fig. 12. CO_2 yield in the presence of $\text{Cu}_{2-x}\text{Se}/\text{Cu}_2\text{O}$ in a continuous flow system: (a) Mineralization of formaldehyde with increased initial concentration, 10 ppm, 20 ppm, 50 ppm; (b) Successive degradation of 50 ppm per 40 min in 8 h; (c) A scheme that illustrates reaction between HCHO and radicals. (Total volume: 8 L; Flow rate: 0.6 L/min).



Scheme 1. (a) A rolled $\text{Cu}_{2-x}\text{Se}/\text{Cu}_2\text{O}/\text{Cu}$ mesh and appearance of a typical air purifier, (b) exploded view of the air purifier with $\text{Cu}_{2-x}\text{Se}/\text{Cu}_2\text{O}/\text{Cu}$ mesh as photocatalyst; (c) schematic diagram of tube-in-tube construction and air circumfluence inside $\text{Cu}_{2-x}\text{Se}/\text{Cu}_2\text{O}/\text{Cu}$ mesh tube. (1 motor, 2 outlet, 3 baffle, 4 low power lamp, 5 fixed shaft, 6 rolled $\text{Cu}_{2-x}\text{Se}/\text{Cu}_2\text{O}/\text{Cu}$ mesh, 7 buffer tube, 8 bracket, 9 HEPA, 10 impeller, 11 air inlet).

4. Conclusion

Mineralization of HCHO conducted on a three-dimensional self-

supporting $\text{Cu}_{2-x}\text{Se}/\text{Cu}_2\text{O}$ crystals was studied. Nonstoichiometric Cu_{2-x}Se nanoplates spontaneously grow from a Cu mesh that serves as Cu source and substrate, which intersect each other to form an organized

flower-like structure characterized by a porous interface. Subjecting Cu_{2-x}Se to calcination in O₂/N₂ atmosphere enables the in-situ substitution of Se with O, leading to the formation of Cu_{2-x}Se/Cu₂O heterojunction implanted in Cu_{2-x}Se nanoplates. Calculation validates the shared Cu atoms between Cu_{2-x}Se and Cu₂O lattices are anchor points to firmly adsorb O₂, H₂O and HCHO. Moreover, as Cu_{2-x}Se and Cu₂O are p-type semiconductors with a small bandgap, they construct a p-p heterojunction, offering countless photo-induced electrons to Cu_{2-x}Se/Cu₂O surface. The electron-enriching interface converts O₂ to active oxygen species for the timely oxidation of those activated HCHO-intermediates, realizing the rapid and complete elimination of hazardous HCHO.

Photocatalysis based on semiconductors applied for removing environmental pollutants from both air and water matrices has been studied for over 40 years. Although the gap between academic research and industrial applications is still wide, self-supporting photocatalysts have the most promising future because of the following advantages. First, the desirable crystals were in-situ grown on a conductive substrate, avoiding the filming operation and simplifying the application process. Second, the integrated feature renders it an ideal substrate for further engineering or rivet other guest catalysts. In addition, the intimate contact between the catalyst layer and its substrate guarantees fast charge transfer, facilitating the separation of photogenerated hole-electron pairs. Just like Cu_{2-x}Se described herein, the all-solid Cu_{2-x}Se/Cu₂O/Cu mesh figures out the attractive prospect of photocatalysis in air purification and closes the gap between scientific reports and practical application.

CRediT authorship contribution statement

Wei Liu: Methodology, Investigation, Writing. **Mengyi Shi:** Investigation. **Yingting Li:** Design. **Ziyi Wu:** Investigation. **Lixia Yang:** Supervision, Writing – review & editing. **Shuqu Zhang:** Methodology. **Xiao Xiao:** Methodology. **Chengjin Liu:** Methodology. **Weili Dai:** Supervision, Methodology. **Congjing Chen:** Conceptualization. **Xinman Tu:** Resources. **Jianping Zou:** Resources. **Xubiao Luo:** Resources.

Declaration of Competing Interest

The authors declare that they have no known competing financial interests or personal relationships that could have appeared to influence the work reported in this paper.

Acknowledgments

This work was supported by the National Natural Science Foundation of China (52070092, 52072165). We are grateful for the financial support received for this project. The authors would also like to thank Shiyanjia (www.shyanjia.com) for the support of in situ FTIR analysis.

Appendix A. Supporting information

Supplementary data associated with this article can be found in the online version at [doi:10.1016/j.apcatb.2022.121427](https://doi.org/10.1016/j.apcatb.2022.121427).

References

- [1] N.E. Klepeis, W.C. Nelson, W.R. Ott, J.P. Robinson, A.M. Tsang, P. Switzer, J. V. Behar, S.C. Hern, W.H. Engelmann, The National Human Activity Pattern Survey (NHAPS): a resource for assessing exposure to environmental pollutants, *J. Expo. Anal. Environ. Epidemiol.* 11 (2001) 231–352, <https://doi.org/10.1038/sj.jea.7500165>.
- [2] W. Bank, IfH Metrics, Evaluation, The cost of air pollution: strengthening the economic case for action, World Bank, 2016, <https://doi.org/10.1596/25013>.
- [3] Y. Liu, M. Shao, L. Fu, S. Lu, L. Zeng, D. Tang, Source profiles of volatile organic compounds (VOCs) measured in China: Part I, *Atmos. Environ.* 42 (25) (2008) 6247–6260, <https://doi.org/10.1016/j.atmosenv.2008.01.070>.
- [4] J. Jin, P. Li, D.H. Chun, B. Jin, K. Zhang, J.H. Park, Defect dominated hierarchical ti-metal-organic frameworks via a linker competitive coordination strategy for toluene removal, *Adv. Funct. Mater.* 31 (32) (2021) 2102511–2102518, <https://doi.org/10.1002/adfm.202102511>.
- [5] B. Kim, Y.R. Lee, H.Y. Kim, W.S. Ahn, Adsorption of volatile organic compounds over MIL-125-NH₂, *Polyhedron* 154 (2018) 343–349, <https://doi.org/10.1016/j.poly.2018.08.010>.
- [6] Z. Dai, J. Zhu, J. Yan, J. Su, Y. Gao, X. Zhang, Q. Ke, G.N. Parsons, An advanced dual-function MnO₂-fabric air filter combining catalytic oxidation of formaldehyde and high-efficiency fine particulate matter removal, *Adv. Funct. Mater.* 30 (42) (2020) 2001488–2001499, <https://doi.org/10.1002/adfm.202001488>.
- [7] Y. Guo, M. Wen, G. Li, T. An, Recent advances in VOC elimination by catalytic oxidation technology onto various nanoparticles catalysts: a critical review, *Appl. Catal. B: Environ.* 281 (2021) 119447–119465, <https://doi.org/10.1016/j.apcatb.2020.119447>.
- [8] T.A. Chang, C.L. Ma, Z.X. Shen, S.K.P. Veerapandian, Y. Huang, N. De Geyter, R. Morent, Mn-based catalysts for post non-thermal plasma catalytic abatement of VOCs: a review on experiments, simulations and modeling, *Plasma Chem. Plasma Process* 41 (5) (2021) 1239–1278, <https://doi.org/10.1007/s11090-021-10195-2>.
- [9] P. Wu, X. Jin, Y. Qiu, D. Ye, Recent progress of thermocatalytic and photo/thermocatalytic oxidation for VOCs purification over manganese-based oxide catalysts, *Environ. Sci. Technol.* 55 (8) (2021) 4268–4286, <https://doi.org/10.1021/acs.est.0c08179>.
- [10] V. Boonamnuayvitaya, S. Sae-ung, W. Tanthapanichakoon, Preparation of activated carbons from coffee residue for the adsorption of formaldehyde, *Sep. Purif. Technol.* 42 (2) (2005) 159–168, <https://doi.org/10.1016/j.seppur.2004.07.007>.
- [11] G. de Falco, W. Li, S. Cimino, T.J.J.C. Bandosz, Role of sulfur and nitrogen surface groups in adsorption of formaldehyde on nanoporous, *Carbons* 138 (2018) 283–291, <https://doi.org/10.1016/j.carbon.2018.05.067>.
- [12] J. Yu, X. Li, Z. Xu, W. Xiao, NaOH-modified ceramic honeycomb with enhanced formaldehyde adsorption and removal performance, *Environ. Sci. Technol.* 47 (17) (2013) 9928–9933, <https://doi.org/10.1021/es401989z>.
- [13] X. Tang, J. Chen, Y. Li, Y. Li, Y. Xu, W. Shen, Complete oxidation of formaldehyde over Ag/MnO_x-CeO₂ catalysts, *Chem. Eng. J.* 118 (1–2) (2006) 119–125, <https://doi.org/10.1016/j.cej.2006.02.002>.
- [14] X. Zhu, X. Gao, R. Qin, Y. Zeng, R. Qu, C. Zheng, X.J.A.C.B.E. Tu, Plasma-catalytic removal of formaldehyde over Cu–Ce catalysts in a dielectric barrier discharge reactor, *Appl. Catal. B: Environ.* 170 (2015) 293–300, <https://doi.org/10.1016/j.apcatb.2015.01.032>.
- [15] H. Zhou, Z. Wen, J. Liu, J. Ke, X. Duan, S. Wang, Z-scheme plasmonic Ag decorated WO₃/Bi₂WO₆ hybrids for enhanced photocatalytic abatement of chlorinated-VOCs under solar light irradiation, *Appl. Catal. B: Environ.* 242 (2019) 76–84, <https://doi.org/10.1016/j.apcatb.2018.09.090>.
- [16] D. Zhu, M. Chen, Y. Huang, R. Li, T. Huang, J. Cao, Z. Shen, S.C. Lee, FeCo alloy encased in nitrogen-doped carbon for efficient formaldehyde removal: Preparation, electronic structure, and d-band center tailoring, *J. Hazard. Mater.* 424 (2022), <https://doi.org/10.1016/j.jhazmat.2021.127593>.
- [17] R. Li, Y. Huang, D. Zhu, W.K. Ho, J. Cao, S.C. Lee, Improved oxygen activation over a carbon/Co₃O₄ nanocomposite for efficient catalytic oxidation of formaldehyde at room temperature, *Environ. Sci. Technol.* 55 (6) (2021) 4054–4063, <https://doi.org/10.1021/acs.est.1c00490>.
- [18] J. Ye, M. Zhou, Y. Le, B. Cheng, J. Yu, Three-dimensional carbon foam supported MnO₂/Pt for rapid capture and catalytic oxidation of formaldehyde at room temperature, *Appl. Catal. B: Environ.* 267 (2020) 118689–118697, <https://doi.org/10.1016/j.apcatb.2020.118689>.
- [19] W. Song, L. Chen, L. Wan, M. Jin, Z. Li, The influence of doping amount on the catalytic oxidation of formaldehyde by Mn-CeO₂ mixed oxide catalyst: A combination of DFT and microkinetic study, *J. Hazard. Mater.* 425 (2022), <https://doi.org/10.1016/j.jhazmat.2021.127985>.
- [20] R. Chen, J. Li, H. Wang, P. Chen, X. Dong, Y. Sun, Y. Zhou, F. Dong, Photocatalytic reaction mechanisms at a gas–solid interface for typical air pollutant decomposition, *J. Mater. Chem. A* 9 (2021) 20184–20210, <https://doi.org/10.1039/DITA03705F>.
- [21] T. Noguchi, A. Fujishima, P. Sawunyama, K. Hashimoto, Photocatalytic degradation of gaseous formaldehyde using TiO₂ film, *Environ. Sci. Technol.* 32 (1998), <https://doi.org/10.1021/es980299>.
- [22] G. Zhang, Z. Sun, Y. Duan, R. Ma, S. Zheng, Synthesis of nano-TiO₂/diatomite composite and its photocatalytic degradation of gaseous formaldehyde, *Appl. Surf. Sci.* 412 (2017) 105–112, <https://doi.org/10.1016/j.apsusc.2017.03.198>.
- [23] Y. Qin, Z. Wang, J. Jiang, L. Xing, K. Wu, One-step fabrication of TiO₂/Ti foil annular photoreactor for photocatalytic degradation of formaldehyde, *Chem. Eng. J.* 394 (2020), <https://doi.org/10.1016/j.cej.2020.124917>.
- [24] W. Diao, H. Cai, L. Wang, X. Rao, Y.J.C. Zhang, Efficient photocatalytic degradation of gas-phase formaldehyde by Pt/TiO₂ nanowires in a continuous flow reactor, *ChemCatChem* 12 (21) (2020) 5420–5429, <https://doi.org/10.1002/cctc.202000837>.
- [25] Q. Huang, Y. Hu, Y. Pei, J. Zhang, M. Fu, In situ synthesis of TiO₂@NH₂-MIL-125 composites for use in combined adsorption and photocatalytic degradation of formaldehyde, *Appl. Catal. B: Environ.* 259 (2019) 118106–118119, <https://doi.org/10.1016/j.apcatb.2019.118106>.
- [26] L. Kong, X. Li, P. Song, F. Ma, Porous graphitic carbon nitride nanosheets for photocatalytic degradation of formaldehyde gas, *Chem. Phys. Lett.* 762 (2021) 138132–138138, <https://doi.org/10.1016/j.cplett.2020.138132>.
- [27] T. Wang, Y. Wang, M. Sun, A. Hanif, H. Wu, Q. Gu, Y.S. Ok, D.C.W. Tsang, J. Li, J. Yu, J. Shang, Thermally treated zeolitic imidazolate framework-8 (ZIF-8) for visible light photocatalytic degradation of gaseous formaldehyde, *Chem. Sci.* 11 (26) (2020) 6670–6681, <https://doi.org/10.1039/d0sc01397h>.

- [28] L. Yang, J. Guo, T. Yang, C. Guo, S. Zhang, S. Luo, W. Dai, B. Li, X. Luo, Y. Li, Self-assembly Cu₂O nanowire arrays on Cu mesh: a solid-state, highly-efficient, and stable photocatalyst for toluene degradation under sunlight, *J. Hazard. Mater.* 402 (2021), <https://doi.org/10.1016/j.jhazmat.2020.123741>.
- [29] L. Yang, J. Guo, J. Zhang, S. Zhang, W. Dai, X. Xiao, X. Luo, S. Luo, Utter degradation of toluene with inhibiting the generation of benzene by self-supporting Bi₂MoO₆ nanoflakes featuring OV-enriched interface, *Chem. Eng. J.* 427 (2022) 131550–131563, <https://doi.org/10.1016/j.cej.2021.131550>.
- [30] A.M. Hermann, L. Fabick, Research on polycrystalline thin-film photovoltaic devices, *J. Cryst. Growth* 61 (3) (1983) 658–664, [https://doi.org/10.1016/0022-0248\(83\)90195-1](https://doi.org/10.1016/0022-0248(83)90195-1).
- [31] R.H. Bari, V. Ganesan, S. Potadar, L.A. Patil, Structural, optical and electrical properties of chemically deposited copper selenide films, *B. Mater. Sci.* 32 (1) (2009) 37–42, <https://doi.org/10.1007/s12034-009-0006-z>.
- [32] J. Xu, W. Zhang, Z. Yang, S. Ding, C. Zeng, L. Chen, Q. Wang, S. Yang, Large-scale synthesis of long crystalline Cu_{2-x}Se nanowire bundles by water-evaporation-induced self-assembly and their application in gas sensing, *Adv. Funct. Mater.* 19 (11) (2009) 1759–1766, <https://doi.org/10.1002/pssa.201026288>.
- [33] X. Liu, W.C. Law, M. Jeon, X. Wang, M. Liu, C. Kim, P.N. Prasad, M.T. Swihart, Cu_{2-x}Se nanocrystals with localized surface plasmon resonance as sensitive contrast agents for *in vivo* photoacoustic imaging: Demonstration of sentinel lymph node mapping, *Adv. Funct. Mater.* 2 (7) (2013) 952–957, <https://doi.org/10.1002/adhm.201200388>.
- [34] H. Li, J. Jiang, F. Wang, J. Huang, Y. Wang, Y. Zhang, J. Zhao, Facile synthesis of rod-like Cu_{2-x}Se and insight into its improved lithium-storage property, *ChemSusChem* 10 (10) (2017) 2235–2241, <https://doi.org/10.1002/cssc.201700317>.
- [35] Y. Liu, S. Shen, J. Zhang, W. Zhong, X. Huang, Cu_{2-x}Se/CdS composite photocatalyst with enhanced visible light photocatalysis activity, *Appl. Surf. Sci.* 478 (2019) 762–769, <https://doi.org/10.1016/j.apsusc.2019.02.010>.
- [36] G. Kresse, J. Furthmüller, Efficiency of Ab-Initio total energy calculations for metals and semiconductors using a plane-wave basis set, *Comput. Mater. Sci.* 6 (1996) 15–50, [https://doi.org/10.1016/0927-0256\(96\)00008-0](https://doi.org/10.1016/0927-0256(96)00008-0).
- [37] G. Kresse, J. Furthmüller, Efficient iterative schemes for Ab initio total-energy calculations using a plane-wave basis set, *Phys. Rev. B.* 54 (1996) 11169–11186, <https://doi.org/10.1103/PhysRevB.54.11169>.
- [38] Z. Wu, R.E. Cohen, More accurate generalized gradient approximation for solids, *Phys. Rev. B.* 73 (2006) 235116–235121, <https://doi.org/10.1103/PhysRevB.73.235116>.
- [39] G. Kresse, D. Joubert, From ULtrasoft Pseudopotentials to the Projector Augmented-wave Method, *Phys. Rev. B.* 59 (1999) 1758–1775, <https://doi.org/10.1103/PhysRevB.59.1758>.
- [40] P.E. Blöchl, Projector augmented-wave method, *Phys. Rev. B.* 50 (1994) 17953–17979, <https://doi.org/10.1103/PhysRevB.50.17953>.
- [41] S. Grimme, J. Antony, S. Ehrlich, H. Krieg, A consistent and accurate ab initio parametrization of density functional dispersion correction (DFT-D) for the 94 elements H-Pu, *J. Chem. Phys.* 15 (2010) 154104–154123, <https://doi.org/10.1063/1.3382344>.
- [42] G. Henkelman, B.P. Uberuaga, H. Jónsson, A climbing image nudged elastic band method for finding saddle points and minimum energy paths, *J. Chem. Phys.* 113 (2000) 9901–9905, <https://doi.org/10.1063/1.1329672>.
- [43] S.-C. Wu, C.-S. Tan, M.H. Huang, Strong facet effects on interfacial charge transfer revealed through the examination of photocatalytic activities of various Cu₂O-ZnO heterostructures, *Adv. Funct. Mater.* 27 (2017), <https://doi.org/10.1002/adfm.201604635>.
- [44] Y. Zhao, H. Pan, Y. Lou, X. Qiu, J. Zhu, C. Burda, Plasmonic Cu_{2-x}S nanocrystals: optical and structural properties of copper-deficient copper(I) sulfides, *J. Am. Chem. Soc.* 131 (2009) 4253–4261, <https://doi.org/10.1021/ja805655b>.
- [45] I. Kriegel, C. Jiang, J. Rodriguez-Fernandez, R.D. Schaller, D.V. Talapin, E. da Como, J. Feldmann, Tuning the excitonic and plasmonic properties of copper chalcogenide nanocrystals, *J. Am. Chem. Soc.* 134 (2012) 1583–1590, <https://doi.org/10.1021/ja207798q>.
- [46] X. Liu, X. Wang, B. Zhou, W.-C. Law, A.N. Cartwright, M.T. Swihart, Size-controlled synthesis of Cu_{2-x}E (E = S, Se) nanocrystals with strong tunable near-infrared localized surface plasmon resonance and high conductivity in thin films, *Adv. Funct. Mater.* 23 (2013) 1256–1264, <https://doi.org/10.1002/adfm.201202061>.
- [47] N.H. Linh, T.Q. Nguyen, W.A. Diño, H. Kasai, Effect of oxygen vacancy on the adsorption of O₂ on anatase TiO₂(001): a DFT-based study, *Surf. Sci.* 633 (2015) 38–45, <https://doi.org/10.1016/j.susc.2014.11.015>.
- [48] M. Ran, W. Cui, K. Li, L. Chen, Y. Zhang, F. Dong, Light-induced dynamic stability of oxygen vacancies in Bi₂SnO₄ for efficient photocatalytic formaldehyde degradation, *Energy Environ. Mater.* 0 (2021) 1–8, <https://doi.org/10.1002/eem.202100001>.
- [49] M. Chen, H. Wang, X. Chen, F. Wang, X. Qin, C. Zhang, H. He, High-performance of Cu-TiO₂ for photocatalytic oxidation of formaldehyde under visible light and the mechanism study, *Chem. Eng. J.* 390 (2020) 124481–124488, <https://doi.org/10.1016/j.cej.2020.124481>.
- [50] J. Li, W. Cui, P. Chen, X. Dong, Y. Chu, J. Sheng, Y. Zhang, Z. Wang, F. Dong, Unraveling the mechanism of binary channel reactions in photocatalytic formaldehyde decomposition for promoted mineralization, *Appl. Catal. B: Environ.* 260 (2020) 118130–118136, <https://doi.org/10.1016/j.apcatb.2019.118130>.
- [51] J. Yu, S. Wang, J. Low, W. Xiao, Enhanced photocatalytic performance of direct Z-scheme g-C₃N₄-TiO₂ photocatalysts for the decomposition of formaldehyde in air, *Phys. Chem. Chem. Phys.* 15 (2013) 16883–16890, <https://doi.org/10.1039/C3CP53131G>.
- [52] H. Dou, D. Long, X. Rao, Y. Zhang, Y. Qin, F. Pan, K. Wu, Photocatalytic degradation kinetics of gaseous formaldehyde flow using TiO₂ nanowires, *ACS Sustain. Chem. Eng.* 7 (2019) 4456–4465, <https://doi.org/10.1021/acscuschemeng.8b06463>.
- [53] M. Rasander, L. Bergqvist, A. Delin, Density functional theory study of the electronic structure of fluorite Cu₂Se, *J. Phys.: Condens. Matter* 25 (2013) 125503–125510, <https://doi.org/10.1088/0953-8984/25/12/125503>.
- [54] Z. Xu, J. Yu, M. Jaroniec, Efficient catalytic removal of formaldehyde at room temperature using AlOOH nanoflakes with deposited Pt, *Appl. Catal. B: Environ.* 163 (2015) 306–312, <https://doi.org/10.1016/j.apcatb.2014.08.017>.
- [55] J. Low, J. Yu, M. Jaroniec, S. Wageh, A.A. AL-Ghamdi, Heterojunction photocatalysts, *Adv. Mater.* 29 (20) (2017) 1601694–1601713, <https://doi.org/10.1002/adma.201601694>.
- [56] X.H. Chen, Y.T. Chen, F.F. Ren, S.L. Gu, H.H. Tian, C. Jagadish, J.D. Ye, Band alignment and band bending at α -Ga₂O₃/ZnO nm isotype hetero-interface, *Appl. Phys. Lett.* 115 (2019) 202101–202106, <https://doi.org/10.1063/1.5126325>.
- [57] Y. Zhang, L. Qian, W. Ge, P. Lai, X. Liu, Tailoring the band alignment of GaxZn_{1-x}O/InGaZnO heterostructure for modulation-doped transistor applications, *Phys. Status Solidi A* 215 (18) (2018) 1800332–1800336, <https://doi.org/10.1002/pssa.201800332>.
- [58] Z. Bo, X. Guo, X. Wei, H. Yang, J. Yan, K. Cen, Mutualistic decomposition pathway of formaldehyde on O-predosed 8-MnO₂, *Appl. Surf. Sci.* 498 (2019) 143784–143793, <https://doi.org/10.1016/j.apsusc.2019.143784>.
- [59] F.B. Fauzi, E. Ismail, M.H. Ani, S.N.S.A. Bakar, M.A. Mohaned, B.Y. Majlis, M.F. M. Din, M.A.A.M. Abid, A critical review of the effects of fluid dynamics on graphene growth in atmospheric pressure chemical vapor deposition, *J. Mater. Res.* 33 (9) (2018) 1088–1108, <https://doi.org/10.1557/jmr.2018.39>.
- [60] J. Kolarik, P. Wargocki, Can a photocatalytic air purifier be used to improve the perceived air quality indoors? *Indoor Air* 20 (3) (2010) 255–262, <https://doi.org/10.1111/j.1600-0668.2010.00650.x>.